Alternative local melting-solidification of suspended nanoparticles for heterostructure formation enabled by pulsed laser irradiation

Mohammad Sadegh Shakeri[1,], Zaneta Swiatkowska-Warkocka[1], Oliwia Polit[1], Tatiana Itina[2], Alexey Maximenko[3], Joanna Depciuch[1,4], Jacek Gurgul[5], Marzena Mitura-Nowak[1], Marcin Perzanowski[1], Andrzej Dziedzic[6], Jarosław Nęcki[7]*

1. Institute of Nuclear Physics Polish Academy of Sciences, PL-31342 Krakow, Poland
2. Université Jean Monnet Saint-Etienne, CNRS, Institut d Optique Graduate School, Laboratoire Hubert Curien UMR 5516, F-42023, SAINT-ETIENNE, France
3. SOLARIS National Synchrotron Radiation Centre, Jagiellonian University, 30-392 Krakow, Poland
4. Department of Biochemistry and Molecular Biology, Medical University of Lublin, Poland
5. Jerzy Haber Institute of Catalysis and Surface Chemistry, Polish Academy of Sciences, Niezapominajek 8, 30-239 Krakow, Poland
6. College of Natural Sciences, University of Rzeszow, Pigonia 1, 35-310 Rzeszow, Poland
7. AGH University of Science and Technology, Al. Adama Mickiewicza 30, 30-059 Kraków, Poland

* Corresponding Author,
Mohammad Sadegh Shakeri (M.S. Shakeri)
Email: ms.shakeri@ifj.edu.pl
Phone No.: +48 515019092

Keywords: Laser-suspension interaction; Phase formation; Heterostructures; Reactive bond molecular dynamics; ab-initio calculations

Abstract

Phase formation by pulsed laser irradiation of suspended nanoparticles has recently been introduced as a promising synthesis technique for heterostructures. The main challenge still lingers regarding the exact mechanism of particle formation due to the non-equilibrium kinetic by-products resulting from the localized alternative, fast, high-temperature nature of the process. Here, we analyze the bond breaking/formation of copper or copper (II) interfaces with ethanol during the absorption of pulses for Cu-CuO-Cu_2O formation applicable as a electrocatalyst in ethanol oxidation fuel cells. This study includes, but is not limited to, a comprehensive discussion of the interaction between nano-laser pulses and suspension for practical control of the synthesis process. The observed exponential and logarithmic changes in the content of heterostructures for the CuO-ethanol and Cu-ethanol samples irradiated with different fluences were interpreted as the dominant role of physical and chemical reactions, respectively, during the PLIS synthesis. We have also shown that the local interface between dissociated ethanol and the molten sphere is responsible for the oxidative/reductive interactions resulting in the formation of catalytic-augmented Cu^{3+} by-product, thanks to the reactive bond force field molecular dynamics studies confirmed by ab-initio calculations and experimental observations.

1. Introduction

It is no exaggeration to say that the high application potential of the interaction between lasers and matter fascinates the scientific community with new applications every day [1-13]. In this respect, the concept of laser-suspension interaction is not yet fully developed, but it promises a whole range of applications due to the temperature selectivity enabled by the absorption rules. When a suspension is irradiated with a laser pulse, the electromagnetic wave is locally absorbed by the suspended agglomerates, resulting in a temperature rise. Depending on their temperature, possible phase formations/transitions take place in a short time of the pulse duration. Immediately, the particles are cooled to ambient temperature by thermal equilibrium with the solvent molecules, which are transparent to the laser beam. This process is alternatively repeated during pulsed laser irradiation of suspensions (PLIS), initially known as pulsed laser melting in liquid (PLML) [14-20]. In 2007, Ishikawa et al [21] reported for the first time that unlike the laser ablation process used to produce smaller nanoparticles, PLML uses lower laser fluences and forms larger particles than the original constituents by melting. Later, an absorption model was introduced to calculate the temperature of suspended particles irradiated by a pulsed laser [22], followed by the addition of a cooling term to the model to calculate the temperature even more accurately [23]. However, these efforts facilitate the interpretation of thermodynamic phase transitions during PLIS; the undeniable role of the kinetics of the probable chemical reactions has been ignored.

The lower toxicity and low market cost of ethanol make it a suitable source for building fuel cells as promising and advanced energy systems to reduce dependence on fossil fuels [24]. During a complete oxidation scheme of a direct ethanol fuel cell (DEFC), 12 hydroxyl anions are consumed to oxidize ethanol to carbon dioxide and water [25, 26]. Membrane-based acidic and alkaline DEFC types have been developed, with platinum and palladium recognized as the most effective catalysts [27]. Recently, increased efforts have been made to develop low-cost and efficient electrocatalysts to replace the above conventional materials, which suffer from high cost, low abundance, and surface poisoning due to carbon monoxide absorption [28, 29]. To overcome these problems, many works in the literature report the use of copper-based materials, mostly in metallic form [30-36]. The use of copper particles to increase the surface area, which is the most important factor for high catalytic performance, has been limited due to their susceptibility to oxidation under atmospheric conditions. There have been numerous efforts to develop methods to increase the stability of Cu particles by modifying their sensitivity in contact with chemical substances, including the use of alternative Cu-based particles with more complex structures based on copper oxides. Cu-based catalysts can perform a variety of reactions via both one-electron and two-electron pathways because they have a wide range of oxidation states (Cu, Cu(I), Cu(II), and Cu(III)). Therefore, they have found many applications including organic species degradation, electrocatalysis, and photocatalysis. The main

challenge in developing catalytic particles is to develop compounds that are highly active, selective, stable, robust, and cost-effective, which makes Cu/CuO-based particles a suitable candidate for ethanol oxidation fuel cells [37-53].

Here, we first attempted to investigate how the laser/suspension parameters affect particle formation during nano-pulsed laser irradiation of suspended Cu or CuO nanoparticles in ethanol by studying the thermodynamically stable phases using conventional and PLIS-based phase diagrams. The oxidation state of copper was also analyzed experimentally and theoretically to reveal the evolution of Cu-CuO-Cu_2O production as well as the possible formation of kinetic by-products. Besides, reactive bond molecular dynamics (RBMD) was used to study the kinetics of bond breaking/formation when the temperature of the ethanol-particle box is increased. In parallel, we proposed a mathematical model utilizing the laser-suspension parameters to consider the alternative particle growth during the PLIS process. We introduced the high-temperature solvent-sphere interactions, in addition to the physical phase transitions, as the main mechanisms for the PLIS-synthesis of remarkable Cu-CuO-Cu_2O electrocatalysts for ethanol oxidation fuel cells. Exploring the precise role of effective laser-suspension parameters, particle temperature evolution, phase formation mechanism, and alternative particle growth not only makes the PLIS process a preferred controllable synthesis method for heterostructures, but also gives scientists sufficient insight into its potential applications.

2. Results and Discussion

2.1. Phase formation and temperature evolution

Samples are coded according to the nanoparticles they contain and the laser fluence used for their irradiation. In general, there are two groups of Cu-ethanol (Cu50, Cu100, Cu150, and Cu200) and CuO-ethanol (CuO100, CuO200, CuO300, and CuO400) samples synthesized and studied in the present work (Table S1). Powders synthesized by the PLIS method contain Cu, CuO, and Cu_2O phases according to JCPDS No. 003-1018, 48-1548, and 05-0667, respectively (Figure 1a). The change in the intensity of the peaks showed the laser-induced variation in the oxidation state of Cu-CuO-Cu_2O composite. According to the calculated phase diagrams in the Cu-O-C-H system, oxygen pressure plays an important role in the transitions between copper and its oxides ($Log\ P_{O_2} - T$ diagram) when the temperature is high enough to avoid the formation of $Cu(OH)_2$ and $CuCO_3$ phases (Figure 1b). Moreover, the high pressure of CO ($Log\ P_{CO} - Log\ P_{O_2}$ diagram) causes the reduction of the oxide phases and the subsequent formation of metallic Cu (Figure S1). Therefore, it is more likely that Cu, CuO, and Cu_2O and less likely that $Cu(OH)_2$ and $CuCO_3$ are the thermodynamically stable phases that can be crystallized in this system.

The laser fluence (J) required for all possible transitions was calculated for different sizes (D) of Cu and CuO spheres (Figure 1c) according to the phase transitions listed in Table 1. The changes in Gibbs free energy and enthalpy of the probable phases were examined to suggest these transitions

(Figure S2). Similarly, the dielectric constant was manipulated in a way to show the flexible phase boundaries created by the dynamic absorption efficiency at high temperatures. The dynamic absorption during the PLIS process was calculated from the difference between the refractive indices of the particles in ethanol and in vacuum (Figure S3). The temperature profile calculated from the data in Table S2 (Figure 1d) shows that the contribution of energy absorption dominates in the first and middle thirds of the Gaussian pulse, while heat dissipation predominates in the last third (Figure S4). Therefore, pulse shape and pulse duration are responsible for the conservation of energy and heat dissipation, respectively. On the other hand, nanoscale Cu and CuO particles experience the highest temperatures of 2843 and 2858 K, respectively, while according to the maximum temperature calculations, there is an inverse relationship between temperature and submicron particle size (Figure 1e).

2.2. Evaluation of oxidation states

The peak at 212 cm^{-1} of Raman spectra (Figure 2a,b), corresponding to the $2E_u$ phonon mode, is produced by the twisting of Cu_4O tetrahedron around the c-axis of Cu_2O. There are also all three visible phonon modes of CuO, i.e., A_g mode centered at 280 cm^{-1}, B_g at 325 cm^{-1}, and $2B_g$ at 610 cm^{-1}. The T_{1u} modes of Cu_2O and/or bis-μ-oxo dimer core vibration of CuO_2^- (Cu (III)) also oscillate at 610 cm^{-1} [54, 55]. Raman spectra showed greater formation of Cu_2O in the higher fluence irradiated CuO-ethanol samples and maximization of Cu_2O in Cu150 among Cu-ethanol samples.

The binding energy (BE) in the range of 925-960 eV reveals complex spectral features of the Cu 2p photoelectron spectrum (Figure 2c,f). In addition to the well-separated spin-orbit peaks with total momentum j = 3/2 and j = 1/2, there are much weaker additional structures in between associated with shake-up satellites. It is worth noting that shake-up satellites of varying intensity can only be observed for Cu^{2+}, which has a d^9 configuration in the ground state, and they can occur when outgoing photoelectrons interact with valence electrons excited to higher energy levels. The shake-up satellites do not occur in d^{10} Cu^0 or Cu^+ spectra. Unfortunately, it is not possible to distinguish between Cu^0 and CuO, as well as between $Cu(OH)_2$ and Cu_2O, because the chemical shift of the Cu $L_3M_{45}M_{45}$ band is very small.

Four doublets were used to properly fit the Cu 2p spectra (Figure 2c,f). The spin-orbit splitting of all doublets was in the range of 19.7-19.9 eV. The most intense components come from the metallic Cu^0 and Cu_2O species (932.5-932.9 eV), octahedral CuO (933.3-934.0 eV), and Cu^{2+} hydroxide species (>935.0 eV) [56-58]. The weakest doublet (<5.6 %) with Cu $2p_{3/2}$ BE values of 930.9-931.6 eV is caused by the differential charging of the supported Cu particles compared to the silica support surface. A similar phenomenon has already been observed for metallic ruthenium on MgO and SiO_2 [59] and for Ru/Ce systems on mesocellular silica foam [60] and explained as a final state effect due to the higher internal conductivity of the supported Ru compared to the conductivity of the dielectric support.

The kinetic energy of the Cu L3M45M45 Auger peaks was calculated for two main contributions marked by arrows in Figure 2d,g. The first contribution shows the Auger parameter of copper near 1849.1 eV, which is consistent with Cu_2O in the literature [61-64]. The second contribution shows the Auger parameter near 1851.6 eV for all measured samples. According to Biesinger et al [61, 65], the distinction between Cu^0 (1851.2 eV for metallic Cu) and Cu^{2+} species (1851.3 eV for CuO and 1850.9 eV for $Cu(OH)_2$) is almost impossible. Therefore, the second contribution should be treated as coming from metallic copper and Cu^{2+} oxide species together (and marked in this way in Figure 2c,f).

The O 1s spectra (Figure 2e) of Cu-ethanol samples show four components: (I) a peak at 529.9-530.7 eV related to oxygen in copper oxides (CuO and Cu_2O), (II) a peak assigned to hydroxyl groups and $Cu(OH)_2$ (BE = 531.5-531.9 eV), (III) adsorbed water (BE = 532.6-533.7 eV), and (IV) a weak contribution at BE > 534.6 eV that can be attributed to oxygen in organic impurities [57, 61]. Exactly the same components are visible in the O 1s spectra of CuO-ethanol samples (Figure 2h). It is worth noting that only one component corresponding to Cu^0 and Cu^{2+} species is visible in the CuLMM spectrum of the CuO-raw sample. The absence of a component corresponding to Cu^+ species is reflected in the O 1s spectrum as a shift of the component with BE = 529.9 eV to lower values of binding energy compared to the other samples (530.6-531.0 eV). The shift to lower BE values of the component corresponding to Cu_2O and CuO is also evident in the Cu50 spectrum.

Several contributions were found in the C 1s core lines of the studied samples (Figure S5 and Table S3). The organic contaminants (285.0 eV), C-O groups (285.9-286.6 eV), and C=O groups (287.9-288.8 eV) were the components with the highest contribution to each spectrum. In addition, a small amount of carbides and a significant amount of O-C=O groups (289.1-290.0 eV) were found. The hydrocarbon impurities were used as internal calibration for our samples, as mentioned above.

From the above facts, we conclude that a much stronger shake-up satellite accompanied by a Cu 2p peak in XPS spectra is associated with more Cu^{2+} species [56, 65]. Moreover, the absolute BE of Cu 2p peaks do not allow us to distinguish between Cu^+ and Cu^0 oxidation states and between octahedral Cu^{2+} and Cu^+, since the differences between their energies are small [61-63]. In such a case, the distinction between Cu^+ and Cu^0 species can be derived from Wagner's Cu $2p_{3/2}$ – Cu $L_3M_{45}M_{45}$ diagram [61, 64]. Thus, to investigate the oxidation states quantitatively, we used information from high-resolution spectra of Cu 2p (Figure 2c,f), Cu $L_3M_{45}M_{45}$ (Figure 2d,g), and O 1s (Figure 2e,h) regions simultaneously. The main photoelectron peaks of Cu 2p are accompanied by strong shake-up satellites in Cu50 and CuO-RAW samples confirming the presence of copper mainly as Cu^{2+} species [66, 67]. On the other hand, the weakest satellites are observed in the spectra obtained for Cu150 and CuO400, reflected in the smallest area of the sum of their CuO and $Cu(OH)_2$ components (Cu^{2+} content), which is less than 37 % of the total Cu 2p area. In Cu-ethanol samples, an increase in the low oxidation states (Cu^0 and Cu^+) was observed with increasing laser fluence at the expense of a decrease in the Cu^{2+} components (both oxide and hydroxide). For Cu150, the $(Cu^0 + Cu^+)/Cu^{2+}$ ratio

reached a maximum value of 2.9 (Table 2), while among CuO-ethanol samples, it was maximized at about 1.7 for CuO200 and CuO400 (Table 3).

The Cu K-edge absorption spectra includes a pre-edge, an excrescence, and the main peak attributed to $1s \rightarrow 3d$, $1s \rightarrow 4p_z$, and $1s \rightarrow 4p_{x,y}$ transitions, respectively (Figure 2i,j) [68]. Although the $1s \rightarrow 3d$ transition is forbidden according to the dipole selection rules, the pre-edge feature is defined as 3d-4p orbital mixing as well as vibronic and direct quadrupole coupling [69, 70]. The energy of the main peak decreases with laser fluence, while the excrescence energy is constant in all samples. However, the pre-edge shift behaves inconsistently, i.e., it increases for Cu-ethanol samples and decreases for CuO-ethanol samples (Table S4), which is attributed to Cu oxidation and CuO reduction, respectively. Consequently, greater copper oxidation shifts the pre-edge to higher energies and vice versa.

Linear combination fitting (LCF) of composite powders showed wall-to-wall conformance when Cu, CuO, and Cu_2O reference spectra were utilized (Figure 3a-f). It also showed the enrichment of Cu and Cu_2O and the reduction of CuO with increasing laser fluence in both sample groups, which fully confirms the extracted results of XPS (Table S5). Using the LCF, we concluded that phase transformations progress from the center of CuO particles toward the surface, with physical transitions being the major contributor. In contrast, for Cu, the phase transformations proceed from the surface to the center of the particles, with chemical oxidation/reduction interactions accounting for most of the transitions (Figure 3g).

We also calculated the extended X-ray absorption fine structure (EXAFS) spectra of the possible phases using the ab initio Green function (GW) approximation (Figure S6). The Gaussian fit of the X-ray absorption near edge structure (XANES) spectra of all calculated models and measured samples (Figure S7) is summarized in Table S6.

2.3. Molecular dynamics study

We observed the increasing traces of ethylene, methane, ethane and carbon monoxide by laser fluence in the chromatograph chamber (Table 4). These compounds are formed by dissociation of ethanol, although we know that the solvent is transparent to the laser beam. Therefore, we decided to investigate the particle-solvent interaction by means of reactive bond molecular dynamics (RBMD) simulations to support the hypothesis that phase formation during the PLIS process occurs not only through thermodynamic phase transitions, but also through oxidation/reduction processes induced by the interactions between dissociated solvent and molten sphere.

According to the RBMD simulation (Table S7), the interaction between the solvent and the solid phase starts with the absorption of ethanol at the solid surface (Supplementary Video1). In the correlated MB1 simulation box (Figs. S8), the decomposition of ethanol begins with the absorption of the separated OH^- groups on the Cu surface. The remaining C_2H_5 is decomposed to C_2H_4, followed by the formation of smaller hydrocarbons (Figure 4a). The behavior of CuO in the MB2 simulation

box, on the other hand, is different, since the decomposition of the solvent begins with the splitting off of H^+ and its subsequent adsorption on the oxide surface (Figure 4b). The stronger tendency to react with oxygenated anions and hydrogenated cations is the main difference between the behavior of Cu and CuO heated spheres, respectively (Table S8). The reason for observing such a difference is attributed to the basic tendency of Cu^0/Cu^{2+} to be oxidized/reduced in ethanol, depending on the oxygen content of the box, which is also confirmed by DFT calculations (Supplementary part f) [71-76].

According to the results of DFT, the calculated absorption energies of ethanol on the surfaces of Cu (111) and CuO (111) indicate that metallic copper, due to its higher oxidation tendency, is more willing to absorb ethanol by combining with both oxygen and hydrogen of the OH group. CuO, on the other hand, absorbs only the H atom of the OH group with a comparatively smaller tendency. The band gap of CuO was calculated to be 1.45 eV, which is in good agreement with the literature. Moreover, the density of states of ethanol does not affect the band gap of CuO and there is no state in the gap. On the other hand, the denser states of copper correspond to the density of states of ethanol; therefore, ethanol obviously affects the DOS of Cu.

By changing the temperature of the simulation box (MB3 and MB4 models), the only difference detected was the ethanol decomposition rate, which was found to be 0.60, 5.35, and 55.42 molecules/ps for the solvents decomposed at 1000, 1500, and 2843 K, respectively. The same difference was observed when the temperatures of the solvent and the sphere were different (Figure 4c,d). As the model with the lowest decomposition rate, absorption penetration, mixing and chemical reactions of ethanol and hydroxyl cleavage were observed on the surface of MB6 model throughout the simulation period. Consequently, the temperature change influences the phase formation by changing the decomposition rate of the solvent.

Considering the statistical analysis in terms of the new species timeline (MB7 model), oxidation evolution proceeds through (I) ethanol absorption on the Cu surface, (II) hydroxyl cleavage of ethanol, (III) formation of Cu clusters during copper melting, (IV) surface oxidation with hydrogenated compounds, (V) decomposition of C_2H_5 into smaller hydrocarbons, and (VI) net oxidation (Table S9). Ethanol decomposition for the CuO-ethanol system is accelerated compared to the Cu-ethanol system (Figure 4e). Statistical analysis also showed that surface oxidation begins with the absorption of hydroxyl and water molecules by Cu clusters (Figure S9). Later, the hydrogen is separated and the oxygen forms bonds with several copper atoms to achieve net oxidation (Supplementary Video 2). In the simulations, corresponding correlations were observed for both the pressure tensor and the dipole moment (Figure S10). Time-dependent snapshots of the MB1 cross section show deep diffusion of oxygen and hydrogen compounds into the interior of the sphere, while carbon compounds tend to remain in the surface layers. The accumulation of carbon at the surface was also observed in the HAADF-EDX map of particles (Figure 4f).

2.4. Microstructure and particle growth

Analysis of different parts of a given sample by shifting the laser focus in Raman spectroscopy revealed widespread changes in the intensity of Raman shifts (Figure S15). The synchronization between PLIS-based phase diagrams (Figure 1c,e) and the size distribution of the resulting particles (Figure 5a-h) indicated the possible crystallization of different phases, which was also confirmed by HRTEM analysis (Supplementary part h).

To examine particle formation during the PLIS process in more detail, we have attempted to derive a series of equations to see how particles grow during the PLIS process (Supplementary Part j). According to this model, the agglomerates are irradiated with a laser pulse, which leads to fusion and formation of larger particles (Figure 5k). Since the repetition rate of the pulsed laser irradiation is low here, these particles can form new agglomerates, which with a certain probability can be irradiated by another laser pulse, leading to new growth up to a size that can be melted by the laser beam [18]. The calculated probability of the probe (X) showed that the different sizes of Cu agglomerates are irradiated almost between 1 to 2 times, while CuO agglomerates are irradiated between 1 to 3 times (Figure 5i,j). The calculation of $X \geq 1$ rejected the hypothesis of the presence copper which was calculated by LCF of EXAFS spectra as the residual phase. The difference between the average size of the agglomerates and the particles for the particles obtained from the Cu50 sample is due to the small size of the particles and their tendency to agglomerate more. Moreover, the difference between the maximum size of the melted particles and the average size of the agglomerates is due to the fact that more than 1 hour of irradiation at higher laser fluence is required for these two parameters to have the same value (Table 5).

The formation of the necking zone observed mainly in the low fluence irradiated samples (Figure 5l-o) was also simulated by the MB9 model (Figure 5p). Here, the atoms involved in the bond breaking/formation process move towards the center of the simulation box, while the necking zone between two spheres is observed first (Supplementary Video3). Finally, multistage modeling (MB10 and MB11 models) showed a more complete dissociation of the solvent due to the increased formation of H_2, H_2O, CO, and C_2 molecules compared to the previous stage (Figure S12). Furthermore, solvent degradation accelerated with increasing number of stages, indicating greater net oxidation (Figure S13). The stronger dissociation of the solvent molecules in the multistage models (MB10, MB11) allows the carbon species to diffuse deep into the particle interior; therefore, there would be no carbon shell on the surface of the particle as previously observed in the single-stage simulation boxes (MB1, MB2). This suggests that the alternative nature of the process is not only responsible for the growth of the particles, but also for the oxidation/reduction process leading to the removal of the carbon shell, which is also confirmed by EDX measurements on larger particles (Figure S20).

2.5. Possible formation of Cu_2O_3

In some SAED patterns (Figure 6a), we detected d-spacing around 3.25 Å, indicating a possible trace of a different oxidation state of copper [55]. A high-resolution XRD pattern also proved the existence of a characteristic peak at 2θ=27.5° (Figure 6b) attributed to the (111) plane of the orthorhombic Cu_2O_3 phase (Figure 6c). We found that the Cu_2O_3 phase is located at the CuO/Cu_2O interface (Figure 6d) and/or at the surface of the Cu_2O particles (Figure S19). This is mainly due to the formation of regions of high oxygen content during the crystallization of Cu_2O from CuO, which occurs above 1200 K according to the thermodynamically stable phase diagram (Figure 1b).

2.6. Electrocatalysis of ethanol oxidation

The electrochemically active surface area (ECSA) showing hydrogen absorption region calculated from the cyclic voltammogram curves (CV) (Figure 7a) showed the highest mass activity [77, 78] of 5065.00 cm^2/mg_{Cu} and 2037.50 cm^2/mg_{Cu} for CuO200/C and Cu200/C catalysts, respectively (Table S14). Moreover, the best catalytic properties were observed for the Cu100/C and Cu200/C catalysts. In general, Cu-ethanol/C catalysts had greater potential for the ethanol oxidation reaction than CuO-ethanol/C catalysts (Figure 7b), which can be attributed to the energy consumption for CuO reduction to metallic Cu [79, 80]. The value of the onset potential was also minimized for Cu100/C and Cu200/C catalysts (Figure S27). As the most effective catalysts, Cu100/C and Cu200/C were investigated by in situ FTIR to reveal the products of ethanol oxidation (Figure 7c,d). The IRRAS spectral peaks corresponding to CO_2 (complete oxidation), CO, CH_3CHO, and CH_3COOH (partial oxidation) [81, 82] are at 2360 cm^{-1}, 2100 cm^{-1}, 1340 cm^{-1}, and 1280 cm^{-1}, respectively (Figure S28). The highest absorption was observed for CO_2 and the ratio of CO_2/CO was measured to be 43 and 1400 for Cu200/C and Cu100/C catalysts, respectively (Figure 7c,d and Table S15). Compared to the Cu200/C catalyst, the Cu100/C catalyst, which consists of smaller particles (larger surface area), produced 4 times more CO_2 and about 10 times less CO, making it the most effective catalyst among all samples (Table S16). The Cu100/C catalyst retains its full oxidation potential even after 12 hours, which was not observed for Cu200/C. Chronoamperometric tests showed 6 times higher current values for Cu100/C compared to Cu200/C (Figure 7e), while accelerated stability tests showed that the durability after 1000 cycles of the analyzed catalysts was 35% better for Cu100/C compared to Cu200/C (Figure 7f-i). These results confirm that the Cu100/C catalyst has higher electrochemical properties comparable to those of commercial products.

To evaluate the selectivity between the carbonate and acetate pathways during EOR, we analyzed the characteristic bands of the carbonates and acetates. The IRRAS spectra collected for the Cu100/C catalyst show a decreasing trend for the acetate compounds and an increasing trend for the carbonate compounds when the potential is increased (Figure S29a). In contrast, the intensity of the signals for the Cu200/C catalyst shows that both the acetate and carbonate compounds increase with increasing

potential (Figure S29b). This indicates less surface contamination of the carbonate compounds for the Cu100/C catalyst. To confirm the electrocatalysis results, the Ag/AgCl reference electrode was replaced by Hg/HgO and the Pt counter electrode was replaced by a carbon electrode, and the same electrocatalytic properties were studied (Supplementary part l.2). Hopefully, the results are in broad agreement with those presented here.

We can conclude that apart from the surface area and compositional changes [83] that introduced the 27.5%Cu-19.2%CuO-53.3%Cu_2O (Cu100/C) sample as an optimal electrocatalyst, the remarkable electrocatalysis measured here is also due to the role of Cu^{3+} ions on the surface of the particles [84]. The higher surface oxide (Cu^{3+}) in transition metal oxides (TMOs) and also the accumulation of charge carriers in the TMO heterojunctions facilitate the adsorption of alcohol, the desorption of decomposed molecules and the cleavage of the C-H bond by lowering the kinetic barrier [85, 86].

3. Conclusions

Suspended agglomerates are heated by the energy absorption of a laser pulse according to their absorption efficiency, depending on the wavelength-dependent absorption cross section calculated by Mie theory. The absorbed energy is directly proportional to the laser fluence and the surface area of the agglomerate. On the other hand, the pulse factors influence the temperature development, so that the pulse shape is responsible for heat conservation, while the pulse duration controls the heat release. Cooling of the particles and re-agglomeration of the irradiated particles occurs in the time between pulses by synergistic agitation of the suspension. In addition, pulse repetition affects particle growth by changing the probability of the probe. The heating-cooling process is repeated depending on the probability of the probe in the system, resulting in alternative particle growth limited by the melting possibility of agglomerates. The size distribution depends on the solvent molecules and the initial size of the nanoparticles, which determines the temperature gradient of the agglomerates. More importantly, the temperature of agglomerates not only determines their thermodynamically stable phases, but also affects the rate of solvent dissociation during interfacial solvent-particle interactions.

Although the solvent bath is at ambient temperature, the kinetic energy of the molecules coming into contact with the surface of the heated particles is very high, resulting in the bond breaking/formation at the interface between the dissociated solvent and the heated particles. The dissociated species diffuse into the sphere where the oxidation/reduction reactions take place according to their nature. In ethanol, the oxygen-hydrogen compounds diffuse deep into the particles, while larger carbon compounds tend to reside in the layers near the interface. So while the inner part of a particle has more to do with oxidation and physical transitions, the outer part is more controlled by chemical oxidation/reduction reactions that lead to the formation of kinetic byproducts. We have proposed PLIS as a method that kinetically controls surface phase formation and is suitable for catalyst synthesis. Here, experimental observations confirmed by DFT and MD simulations showed the formation of a higher oxidation state of copper, i.e., Cu^{3+}, due to the enrichment of oxygen in the

CuO-Cu_2O interface and/or on the surface of the particles, resulting in the observation of excellent electrocatalysis in the ternary Cu-CuO-Cu_2O catalyst. The presented optimal catalyst is able to retain its potential for complete ethanol oxidation even after 12 hours of use. We have presented the PLIS method as a superior synthesis technique for heterostructures, especially when oxidative/reductive reactions play an important role in the synthesis technique. Future advances and better control of the process will be crucial for this technique to be used industrially. We believe that the present novel study dealing with the comprehensive laser-suspension interaction not only provides a basis for heterostructure synthesis by PLIS, but also opens the knowledge gate to the perspective of the discipline.

4. Materials and Methods

4.1. Raw materials, suspension preparation, and irradiation process

Cu (US Research Nanomaterials, 40 nm average size, 99.9% purity, and 5 mM) or CuO (Sigma Aldrich powder, 50 nm average size, 99.5% purity, and 5 mM) nanoparticles (NPs) were dispersed in ethanol (POCH solvent, 99.8% purity) medium to prepare suspensions with a concentration of 0.0027 gr/liter. The prepared suspensions were mixed with an ultrasonic device and the amount of 15 ml was filled into a sealed cell with a transparent quartz window (wavelength of 523 nm). The second harmonic of an unfocused pulsed Nd:YAG laser (λ = 523 nm) with a frequency of 10 Hz was used for irradiation of the mentioned mixtures. Energy densities of 50, 100, 150, and 200 mJ/cm^2.pulse for Cu-ethanol and 100, 200, 300, and 400 mJ/cm^2.pulse for CuO-ethanol samples were used to irradiate colloidal suspensions for 60 minutes (Table S1). Ultrasonic agitation was used during irradiation to prevent undesirable sedimentation of suspended particles/agglomerates.

4.2. Characterizations

The patterns of the crystal structure of the particles were measured with an X-ray diffractometer (XRD, PANalytical X'Pert Pro). The detection was performed with Cu Kα (α = 1.54 Å) radiation at an operating current and voltage of 30 mA and 40 kV, respectively.

The CRM alpha 300R confocal microscope from WITec was used to record Raman spectra. This instrument contained an Olympus MPLAN (100x/0.90NA) objective and a laser with a wavelength of 532 nm. 60 scans were acquired with an integration time of 30 s (a resolution of 3 cm^{-1}). The Raman scattering line of a silicon foil (520.7 cm-1) was used to calibrate the monochromator before analysis. To avoid heat generation from the laser, a very low laser power was used (~ 0.45 mW). As mentioned in the literature, copper-based compounds are generally susceptible to heat-induced phase transitions caused by thermal localization [54, 55]. WitecFour Plus (version 5.3) was used for baseline correction and cosmic ray removal. Also, GRAMS (version 9.2) was used as a tool for peak fitting.

A multi-chamber UHV system was used with an SES R4000, hemispherical analyzer from Gammadata Scienta for X-ray photoelectron spectroscopy (XPS). The core excitation was produced with an X-ray source (non-monochromatic AlK_{α}, 1486.6 eV) equipped with a current emission anode (12 kV and 15 mA). According to the standard ISO 15472:2001 the calibration of the spectrometer was checked. The energy resolution was 0.9 eV at energy of 100 eV and the area of analyzed sample was 5×0.8 mm (4 mm^2). We initially set the pressure in the chamber to about 1×10^{-10} mbar, which was about 2×10^{-9} mbar during the analysis. The C 1s line at BE = 285.0 eV was used to correct the measured spectra. Quantitative analysis was performed by calculating the surface area of each peak (CasaXPS 2.3.23). During the fitting, the Shirley-type background was subtracted. In addition, a combination of Gaussian and Lorentz lines (70:30) was used for curve fitting.

The suspensions obtained from PLIS were precipitated on the sample holder and air-dried for X-ray absorption spectroscopy (XAS) analyzes. Absorbance sieves of finely powdered pure CuO, Cu_2O (purchased from Merck Co.), and Cu foil were also prepared as a reference for calculating the percentage of phases using the linear combination fitting (LCF) method. The X-ray absorption spectra were recorded at the ASTRA beamline of the National Synchrotron Radiation Center in Krakow, Poland (SOLARIS). The spectrum of the Cu metal foil was accurately recorded before each XAS measurement for calibration purposes. Finally, the spectra were imported into the XAS computer software "Athena" for normalization and extraction of the data [87].

The LCF method was evaluated by mathematically fitting the X-ray absorption spectra (XAS) of the resulting composite particles with the same spectra measured for Cu, CuO, and Cu_2O as reference. In this method, which uses the additive nature of the absorption of each species, the proportions of the reference spectra are added to reconstruct the spectrum of choice. However, it can be applied to XANES, XANES derivative, or EXAFS spectra; here we used it for the entire XAS range measured. The total absorption coefficient can be written as the sum of the chemical forms or species as $Sample = \sum f_i(STD_i)$. Here, "Sample" stands for the least square fit to the energy range of the sample spectrum, and f_i stands for the scaling factors applied to each corresponding standard spectrum (STD_i). The scaling factor determined from the LCF indicates the proportion of the individual phases in the analyzed sample. The subroutine of LCF was created with the software Athena (XAS data analysis). Here we performed LCF by fitting the normalized μ(E) spectrum of the composite samples over the reference spectra from 8900 to 9300 eV. The relative weights of the species can vary from 0 to 1 and the absorption edge energies are kept fixed during the analysis.

A dynamic light scattering instrument (Malvern Zetasizer Nano- ZS) was used to measure the hydrodynamic diameter of Cu and CuO nanoparticles. The instrument was equipped with a He-Ne laser operating at λ = 633 nm and a backscatter angle of 173°.

A Hitachi S4800 and a Tescan Vega3 scanning electron microscope (SEM) were used to evaluate the morphology of PLIS-synthesized particles. The average size of particles in each sample was measured by calculating the diameters of 50 randomly selected particles using ImageJ software.

Finally, a FEI Tecnai Qsiris, 200kV transmission electron microscope (TEM) was used to produce the high-resolution images for d-spacing analysis by fast Fourier transform (FFT). Also, the selected area electron diffraction (SAED) patterns and HAADF-EDX maps were extracted to determine the chemical structure more precisely.

4.3. Thermodynamic calculations

The calculations of the thermodynamic equilibrium in the Cu-O-C-H system were carried out with the HSC Chemistry package (ver. 10.x, https://www.hsc-chemistry.com/). This software is also used for accurate calculation of Cp and enthalpy at different temperatures. The reaction pathways of heated Cu and CuO were also extracted from the Gibbs free energy and enthalpy diagrams from HSC Chemistry.

4.4. Temperature calculations

There is a relationship between the laser fluence, the absorption cross section, the particle weight and the enthalpy of the particles as,

$$J\sigma_{abs}^{\lambda}(d) = m_p \Delta H \quad (1)$$

Where, J (J.cm^{-2}pulse^{-1}) is the laser fluence, σ_{abs}^{λ} (cm^2) is the absorption cross-section of particles, m_p (g) is the particle mass, and ΔH (J g^{-1}) is the enthalpy of the particles. The absorbed energy increases the temperature of the particle undergoing thermodynamic phase transitions. Note that in Equation (1) only the main thermal effects are considered, while thermal expansion and possible mechanical effects such as the formation and propagation of pressure waves and possible mechanical fragmentation are neglected here. These simplifications apply to sufficiently small nanoparticles. These issues will be addressed elsewhere.

To calculate the enthalpy of Cu and CuO spheres, the reaction paths must be known. When copper is heated, there are two phase transitions, melting and boiling, so the enthalpy changes as follows.

$$\Delta H = \int_{T_0}^{T_m} C_P^s(T)dT + \Delta H_m + \int_{T_m}^{T_b} C_P^l(T)dT + \Delta H_b \quad (2)$$

here $C_P^s(T)$ and $C_P^l(T)$ (J g^{-1}K^{-1}) are the heat capacities of solid and liquid Cu. Similarly, ΔH_m and ΔH_b (J g^{-1}) are the latent heat of melting and boiling of Cu, which take place at T_m and T_b ($^{\circ}$K), respectively. Finally, T_0 (K) is the ambient temperature which was set to 298 K in all calculations. For CuO (copper oxide (II)), for which the reaction pathway is shown in Table S2, the enthalpy changes as follows.

$$\Delta H = \int_{T_0}^{T_{CuO(s)\rightarrow Cu_2O(s)}} C_P^{CuO(s)}(T)dT + \Delta H_{CuO(s)\rightarrow Cu_2O(s)} + \int_{T_{CuO(s)\rightarrow Cu_2O(s)}}^{T_m} C_P^{Cu_2O(s)}(T)dT + \Delta H_m +$$

$$\int_{T_m}^{T_{Cu_2O(l)\rightarrow Cu(g)}} C_P^{Cu_2O(l)}(T)dT + \Delta H_{Cu_2O(l)\rightarrow Cu(g)} \quad (3)$$

here, $C_p^{CuO(s)}$, $C_p^{Cu_2O(s)}$, and $C_p^{Cu_2O(l)}$ (J $g^{-1}K^{-1}$) are the heat capacities of solid CuO, solid Cu_2O and molten Cu_2O, respectively. Moreover, $\Delta H_{CuO(s)\rightarrow Cu_2O(s)}$, ΔH_m, and $\Delta H_{Cu_2O(l)\rightarrow Cu(g)}$ (J g^{-1}) are the latent heat of CuO(s)-Cu_2O(s) transition, Cu_2O fusion, and Cu_2O(l)-Cu(g) transition occurring at $T_{CuO(s)\rightarrow Cu_2O(s)}$, T_m, and $T_{Cu_2O(l)\rightarrow Cu(g)}$ (K) temperatures, respectively. Figure S2 shows the changing trends of C_p and H for both phases. It also shows the transition temperatures used to design the reaction pathways according to the Gibbs free energy diagrams. The laser fluence is calculated as follows,

$$J = {}^{E_0}/_{A_L} \tag{4}$$

where, E_0 (J $pulse^{-1}$) is the pulse energy; A_L (cm^{-2}) is the cross section of the laser beam. Figure S4 shows the pulse shape and cumulative pulse intensity used in this study. The Gaussian distribution of the pulse shape would be responsible for the heating. The change in the intensity of the laser pulse due to the propagation direction of the laser affects the heat balance, which we will explain in more detail using the heating-cooling model. The absorption cross section of particles, which is responsible for the absorption of electromagnetic radiation, is calculated by the following equation.

$$\sigma_{abs}^{\lambda}(d) = \frac{\pi d^2 Q_{abs}^{\lambda}(d)}{4} \tag{5}$$

here, d is the particle diameter and $Q_{abs}^{\lambda}(d)$ is the absorption efficiency of the particles calculated using scattering techniques. The absorption efficiencies of Cu and CuO particles were calculated as a function of particle diameter using MiePlot software (ver. 4620, http://www.philiplaven.com/mieplot.htm), as shown in Figure S3. The optical parameters used in the MiePlot software are listed in Table S3.

The weight of the spheres is calculated as follows,

$$m_p = \frac{\rho_p (\pi d_p^3)}{6} \tag{6}$$

where, ρ_p (g cm^{-3}) is the particle density.

4.5. Temperature profile calculations

We define a model that takes into account the heating of the particles due to the absorption of the laser beam and the simultaneous cooling due to the heat transfer with the surrounding media. In this model, only conductive heat transfer is considered, since convection around the particles is negligible in the submicrometer range. Conductive heat transfer is expressed as follows;

$$\frac{dq}{dt} = h.\pi d^2(T_t - T_\infty) \tag{7}$$

where, πd^2 is the particle surface area, T(t) is the particle temperature, T_∞ is the temperature of the surrounding liquid (298 K), and h ($Wm^{-2}K^{-1}$) is the heat transfer coefficient defined by Equation (13) as follows,

$$h = \frac{Nu_d.K}{d} \tag{8}$$

where K is the thermal conductivity of the surrounding fluid, Nu_d is the Nusselt number, and d is the particle diameter. The Nusselt number is the ratio of convective heat transfer to conductive heat transfer. In the case of natural convection on a sphere, the Nusselt number is given by Equation (14) as,

$$Nu_d = 2 + \frac{0.589 Ra_d^{0.25}}{[1+(0469/Pr)^{0.56}]^{0.44}} \quad (9)$$

here, Ra_d is the Rayleigh number and Pr is the Prandtl number. For submicron particles, the magnitude of Nusselt number is equal to 2 because the Rayleigh number is negligible in the submicron range. The values of the heat transfer coefficient for ethanol are given in Table S2.

According to the heating-cooling model, the accumulated heat energy in a particle is the difference between the laser energy absorbed by a particle and the energy dissipated by conductive heat transfer,

$$\frac{dE}{dt} = \frac{dE_{abs}}{dt} - \frac{dq}{dt} \quad (10)$$

The amount of absorbed energy as a function of pulse duration is given as follows,

$$\frac{dE_{abs}}{dt} = \frac{Q_{abs}^{\lambda}(d).\pi d^2 J(t)}{4} \quad (11)$$

Matlab software (ver. R2022a, https:// www.mathworks.com/products/new_products/latest_features. html) was utilized for the numerical solution of heating–cooling differential equation using Rung Kutta 4th order derivation (Equation 10).

4.6. Gas Chromatography (GC)

The GC analyzes were performed using an Agilent 6890N gas chromatograph. The levels of carbon dioxide, carbon monoxide, and oxygen in each sample were measured using a micro TCD detector, Porapak Q, and Molsieve 5A packed columns connected in heart-cut mode. Methane, ethane, and ethylene were separated using a micropacked GG alumina column and a FID detector. For high readings of certain gas concentrations (> 100ppm), the GC was calibrated with the gas mixtures produced by Multax, and the accuracy of the concentrations was more than 2% for all gasses. Low concentrations of gasses were referred to the accepted WMO scale with the set of secondary standards. Uncertainties of GC analyzes (single standard deviation), including sampling, sample transfer, and injection repeatability, were as follows: CO_2: 0.5ppm, CO: 0.2ppm, O_2: 0.1%, CH_4: 0.1ppm, C_2H_4: 0.1ppm, and C_2H_4 (or EtO): 0.1ppm.

4.7. Reactive bond force field Molecular Dynamics

A reactive bond force field (RBFF) with Cu/C/H/O parameters [88] was used when using the ReaxFF module of the AMS software package [89] for molecular dynamics simulations (MD). The mentioned RBFF was developed using previously developed potentials for copper and CHO compounds [90-94]. Since the system we studied contains exactly copper, carbon, hydrogen and oxygen and no other element is involved, the RBFF used can be used as a tested interatomic potential in our system. 3-

dimensional systems (Table S11) with rectangular simulation boxes are constructed with the periodic boundary condition in all directions. The size of the cubic simulation boxes is adjusted accordingly to keep the density the same for all systems. The canonical ensemble (NVT) is used for all MD simulations in conjunction with the Nosé-Hoover thermostat with a damping constant of 100 fs. Prior to the RBFF simulations, energy minimization was performed using the conjugate gradient algorithm to optimize the initial geometric configuration. Then the systems were NVT-equilibrated at 298 K for 5 ps. After reaching equilibrium, a series of RBFF-MD simulations is performed for each system (Table S11). In RBFF-MD simulations, the use of high temperatures to accelerate reactions is a common strategy to overcome limited computing power [95-97]. More importantly, the present study is a comparative study of different cases, so the absolute temperature used is less important. A time step of 0.25 fs is used, which has been shown to be suitable for high temperature simulations with ReaxFF MD [95]. The dynamic trajectory and binding data are recorded every 100 frames (25 fs). For analysis of species, a Cutoff value of 0.3 is chosen for the bond order to detect the molecules that form during the simulation. A low Cutoff value is helpful to cover all reactions even those with very short-lived species. Three parallel simulations were run for each simulation box and the average of these simulations was used for further analysis. The reaction pathways (timeline of new species) are analyzed using the Chemical Trajectory Analyzer (ChemTraYzer) scripts [98]. The simulation results were visualized using AMS and Visual Molecular Dynamics (VMD) programs [99].

4.8. Growth model

The details of the particle growth model were explained in supplementary part g. Equation (S21), Equation (S25), and Equation (S18) were used to calculate Figure 4i, Table S16, and Figure 4j, respectively.

4.9. Ab-initio calculations

Quantum Espresso (QE) software was used to calculate the electronic structure and energy minimization of Cu(111) slab-ethanol, CuO(111) slab-ethanol and Cu_2O_3 unit cell models [100-102]. DFT calculations began with atomic modeling. Then the models were relaxed by minimizing the energy of the system. The calculation of the self-consistent field (SCF) was the last step before the post-processing calculations. Post-processing calculations include but are not limited to the band gap (BG), the partial density of states, and adsorption energy. The adsorption energy (E_{ads}) was calculated as follows,

$$E_{ads} = E_{slab\text{-}molecule} - (E_{slab}+E_{molecule}) \quad (12)$$

where $E_{slab\text{-}molecule}$ is the total energy of Cu(111) and CuO(111) surface after ethanol adsorption, E_{slab} is the total energy of the Cu(111) and CuO(001) surface, and $E_{molecule}$ is the total energy of the isolated ethanol molecule.

A vacuum layer (20 Å) is also added to each slab-containing model to avoid the effect of periodicity of the structure in heterojunction. The Perdew-Burke-Ernzerhof (PBE) of the generalized gradient approximation with the Hubbard on-site potential (GGA+U) approximation was utilized as exchange and interaction potentials. The Van der Waals (vdW) correction is adopted to describe long-range vdW interactions and the dipole-dipole interaction is employed in the case of an asymmetric arrangement of species. The cut-off energy of the electronic wavefunction was 600 eV, and the k-space integration is performed according to the Monkhorst-Park scheme fitted to the reciprocal space size of the crystal structure of the models. The geometry optimization of the model is terminated when the force on each ion is not stronger than 0.05 eV. We have used the pseudopotentials Cu.rel-pbesol-dn-kjpaw_psl.0.2.UPF, O.rel-pbesol-n-kjpaw_psl.0.1.UPF, C.rel-pbesol-n-kjpaw_psl.0.1.UPF, H.rel-pbesol-kjpaw_psl.0.1.UPF from http://www.quantum-espresso.org.

In addition, the jfeff10 software (https://times-software.github.io/feff10/) was used to calculate the XAFS and XANES spectra of the probable crystallized phases in this system including Cu, CuO, Cu_2O, Cu_2O_3, $CuCO_3$, and $Cu(OH)_2$. The unit cells of the above phases were relaxed using QE and the final atomic positions were used in jfeff10 for XAS calculations.

4.10. Catalyst preparation

For the electrochemical measurements, the powders obtained from the PLIS process were placed in the functionalized Vulcan XC -72R and the functionalization of the carbon support was carried out as follows. The carbon powder (20 mg) was immersed in a 0.7 M aqueous solution of HNO_3 for 30 minutes at room temperature. The Vulcan XC-72R was rinsed with distilled water to a neutral pH and then dried at 100℃ for 10 h. Prior to addition, the carbon support was heated to 100°C for 1 h under a pure nitrogen atmosphere and oxidized to form surface functional groups. After carbon functionalization, the washed synthesized powders were dispersed in an ultrasonic bath for 30 minutes and finally applied to Vulcan XC -72R, which was added dropwise with vigorous stirring. In the last step, the mixture was mixed over a night under magnetic stirring and the obtained black powder was washed with ethanol and distilled water. Then it was dried at 80°C for 10 h.

4.11. Electrochemical measurements

We used a standard three-electrode electrochemical cell equipped with a potentiostat (BIO-LOGIC SP -200) to measure the electrochemical behavior of catalysts. First, 2 mg of catalyst powder was ultrasonically mixed with 400 µL of isopropyl alcohol, 10 µL of 5 wt% Nafion, and 100 µL of ultrapure water for 30 min to produce a uniform catalyst ink. Then, a glassy carbon electrode (GCE) was polished and 10 µL of the catalyst ink was applied to it. The preparation of a homogeneous working electrode was naturally completed by air-drying the solvent. Cyclic voltammetry measurements (CV) were performed in an ethanol-containing solution to determine the EOR activity

of the catalysts. Pt as counter electrode and silver chloride as reference electrode were used in a standard glass cell. Before measurements, the electrolyte of 0.1 M NaOH and 0.5 M C_2H_5OH was deoxygenated for 30 minutes by Ar flushing. To show the durability of the studied catalysts, a chronoamperometric test in 0.1 M NaOH and 0.5 M C_2H_5OH at 0.5 V potential was also performed. In addition, accelerated stability tests of the synthesized catalysts were performed by consecutive sweeps from -1 to 1.5 V at 100 mV/s for 1000 potential cycles in 0.1 M NaOH solution. All numerical potentials reported in this study were measured with respect to the reversible hydrogen electrode (RHE) at room temperature.

4.12. The Infrared Reflection Absorption Spectroscopy (IRRAS) measurements

Spectroelectrochemical ATR-FTIR in situ measurements were performed using a NicoletiS50 FT-IR spectrometer equipped with an MCT detector cooled with liquid N2, an ATR accessory with ZnSe crystal, and an electrochemical cell. The working electrodes are the same as those used in electrochemical experiments. Spectra were calculated from 64 scans with a spectral resolution of 2 cm^{-1}, in the IR range between 1200 cm^{-1} and 3000 cm^{-1}. Measurements were performed for 12 h, and the spectrometer was rinsed with Ar 1 h before the experiment. In addition, argon gas was used permanently during these 12 h. The kinetics curves of the peaks were determined for every 30 minutes. The curves were indexed for peaks corresponding to CO_2, CO, CH_3CHO, and CH_3COOH to show the dynamics of the EOR products. To show the selectivity of the catalysts in the reduction of ethanol to carbonate and acetate, the spectra were expressed in absorption units defined as A = -log(R/R0), where R and R0 represent the reflected IR intensities corresponding to the sample and reference single-beam spectra, respectively. The reference spectrum was recorded at 0.05 V in the same solution containing 0.5 M ethanol and 0.1 M NaOH.

Statistical Analysis

All experimental results were analyzed using Excel software. Data were expressed as mean ± standard deviation (SD). In addition, statistical analysis for the formation of new species was performed using the Chemical Trajectory Analyzer (ChemTraYzer) script of the AMS software.

Acknowledgements

This work is mostly supported by the Polish National Science Centre Program No. 2018/31/B/ST8/03043. It is also supported partially by the Polish National Science Centre Program No. 2022/06/X/ST3/01743. The computational works were done in cooperation with Prometheus Cluster, Cyfronet, AGH University of Science and Technology, Krakow using Grant No. PLG/2022/015573. The X-ray absorption spectroscopy measurements were performed at the SOLARIS synchrotron center in Krakow, Poland, under experiment number 221926.

The authors would like to thanks Prof. Marta Marszalek, Dr. Michal Kuprinski, and Dr. Arkadiusz Zarzycki for their support during the whole project. We also are thankful of Dr. Hossein Maleki-Ghaleh, Dr. Ehsan Moradpour Tari, and Prof. Jakub Szlachetko, the Acting Director of the SOLARIS center, due to their consultation for improvement of the scientific relevancy of the current paper. Finally, a special thanks to Prof. Zbigniew Lodziana for accepting to pre-review the paper before submission.

Conflict of Interest

The authors declare no conflict of interest.

References

[1] H. K. Malik, *Laser-matter interaction for radiation and energy*, CRC Press, Boca Raton **2021**.

[2] P. Mulser, D. Bauer, *High power laser-matter interaction*, Springer, Berlin Heidelberg **2010**.

[3] E. Mottay, X. Liu, H. Zhang, E. Mazur, R. Sanatinia, W. Pfleging *MRS Bull.* **2016,** *41*, 984-992.

[4] E. G. Gamaly, S. Juodkazis, K. Nishimura, H. Misawa, B. Luther-Davies, L. Hallo, P. Nicolai, V. T. Tikhonchuk *Phys. Rev. B* **2006**, *73*, 214101.

[5] T.E. Cowan, M. Roth, J. Johnson, C. Brown, M. Christl, W. Fountain, S. Hatchett, E.A. Henry, A.W. Hunt, M.H. Key, A. MacKinnon, T. Parnell, D.M. Pennington, M.D. Perry, T.W. Phillips, T.C. Sangster, M. Singh, R. Snavely, M. Stoyer, Y. Takahashi, S.C. Wilks, K. Yasuike *Nucl. Instrum. Methods Phys. Res.* **2000**, *455*, 130-139.

[6] E. G. Gamaly, *Femtosecond laser-matter interaction: theory, experiments and applications*. Jenny Stanford Publishing, New York **2011**.

[7] H. Lee, Ch. H.J. Lim, M. J. Low, N. Tham, V. M. Murukeshan, Y.-J. Kim *Int. J. Precis. Eng. Manuf.* **2017**, *4*, 307-322.

[8] S.-H. Um, S.-W. Hwang, C. P. Grigoropoulos, H. Jeon, S. H. Ko *Appl. Phys. Rev.* **2022**, *9*, 041302.

[9] A. Thompson *Scilight* **2022**, *2022*, 421106.

[10] M. S. Brown, C B. Arnold, in *Laser Precision Microfabrication*, Vol 135 (Eds: K. Sugioka, M. Meunier, A. Piqué), Springer, Berlin, Heidelberg 2010.

[11] D. J. Joe, S. Kim, J. H. Park, D. Y. Park, H. E. Lee, T. H.g Im, I. Choi, R. S. Ruoff, K. J. Lee *Adv. Mater.* **2017**, *29*, 1606586.

[12] R. Zhou, F. Li, M. Hong *Sci. Sin.: Phys. Mech. Astron.* **2017**, *47*, 024201.

[13] Y. Ishikawa, T. Tsuji, Sh. Sakaki, N. Koshizaki *Prog. Mater. Sci.* **2023**, *131*, 101004.

[14] Y. Ishikawa, N. Koshizaki, A.Pyatenko, N. Saitoh, N. Yoshizawa, Y. Shimizu *J. Phys. Chem. C* **2016**, *120*, 2439-2446.

[15] Y. Ishikawa, N. Koshizaki, Sh. Sakaki *J. Phys. Chem. C* **2019**, *123*, 24934-24942.

[16] A. Pyatenko, H. Wang, N. Koshizaki *J. Phys. Chem. C* **2014**, *118*, 4495-4500.

[17] Y. Ishikawa, Y. Shimizu, T. Sasaki, N. Koshizaki *Appl. Phys. Lett.* **2007**, *91*, 161110.

[18] H. Wang, N. Koshizaki, L. Li, L. Jia, K. Kawaguchi, X. Li, A. Pyatenko, Z. Swiatkowska-Warkocka, Y. Bando, D. Golberg *Adv. Mater.* **2011**, *23*, 1865-1870.

[19] H. Wang, K. Kawaguchi, A. Pyatenko, X. Li, Z. Swiatkowska-Warkocka, Y. Katou, N. Koshizaki *Chem. Eur. J.* **2012**, *18*, 163-169.

[20] M. S. Shakeri, O. Polit, B. Grabowska-Polanowska, A. Pyatenko, K. Suchanek, Mateusz Dulski, J. Gurgul, Z. Swiatkowska-Warkocka *Sci. Rep.* **2022**, *12*, 1-15.

[21] Y. Ishikawa, Y. Shimizu, T. Sasaki, N. Koshizaki *Appl. Phys. Lett.* **2007**, *91*, 161110.

[22] H. Wang, M. Miyauchi, Y. Ishikawa, A. Pyatenko, N. Koshizaki, Y. Li, L. Li, X. Li, Y. Bando, D. Golberg *J. Am. Chem. Soc.* **2011**, *133*, 19102-19109.

[23] Sh. Sakaki, H. Ikenoue, T. Tsuji, Y. Ishikawa, N. Koshizaki *ChemPhysChem* **2017**, 18, 1101-1107.

[24] M. A. F. Akhairi, S K Kamarudin *Int. J. Hydrog. Energy* **2016**, *41*, 4214-4228.

[25] J. Mann, N. Yao, A. B. Bocarsly *Langmuir* **2006**, *22*, 10432-10436.

[26] F. Vigier, C. Coutanceau, A. Perrard, E. M. Belgsir, C. Lamy *J. Appl. Electrochem.* **2004**, *34*, 439-446.

[27] E. Antolini *J. Power Sources* **2007**, *170*, 1-12.

[28] A. V. Munde, B. B. Mulik, P. P. Chavan, V. S. Sapner, S. S. Narwade, S. M. Mali, B. R. Sathe *J. Phys. Chem. C* **2021**, *125*, 2345-2356.

[29] Y. Zheng, X. Wan, X. Cheng, K. Cheng, Z. Dai, Z. Liu *Catalysts* **2020**, *10*, 166.

[30] J. Cai, Y. Zeng, Y. Guo *J. Power Sources* **2014**, 270, 257-261.

[31] Q. Dong, Y. Zhao, X. Han, Y. Wang, M. Liu, Y. Li *Int. J. Hydrog. Energy* **2014**, *39*, 14669-14679.

[32] H. Rostami, A. A. Rostami, A. Omrani *Electrochim. Acta* **2016**, *194*, 431-440.

[33] A. E. Attar, L. Oularbi, S. Chemchoub, M. E. Rhazi *Int. J. Hydrog. Energy* **2020**, *45*, 8887-8898.

[34] J. Biemolt, D. van Noordenne, J. Liu, E. Antonetti, M. Leconte, S. van Vliet, R. Bliem, G. Rothenberg, X.-Z. Fu, N. Yan *ACS Appl. Nano Mater.* **2020**, 3, 10176-10182.

[35] J. Xue, G. Han, W. Ye, Y. Sang, H. Li, P. Guo, X. S. Zhao *ACS Appl. Mater. Interfaces* **2016**, *8*, 34497-34505.

[36] D. Liu, H.-Z. Huang, Z. Zhu, J. Li, L.-W. Chen, X.-T. Jing, A.-X. Yin *Catalysts* **2022**, *12*, 1562.

[37] J. Zhang, J. Liu, Q. Peng, X. Wang, Y Li *Chem. Mater.* **2006**, *18*, 867-871.

[38] B. C. Ranu, R. Dey, T. Chatterjee, S. Ahammed *ChemSusChem* **2012**, *5*, 22−44.

[39] S. E. Allen, R.R. Walvoord, R. Padilla-Salinas, M. C. Kozlowski *Chem. Rev.* **2013**, *113*, 6234−6458.

[40] O. Amadine, H. Maati, K. Abdelouhadi, A. Fihri, S. El Kazzouli, C. Len, A. El Bouari, A. Solhy *J. Mol. Catal. A: Chem*. **2014**, *395*, 409−419.

[41] K. Pan, H. Ming, H. Yu, Y. Liu, Z. Kang, H. Zhang, S.- T. Lee *Cryst. Res. Technol.* **2011**, *46*, 1167−1174.

[42] Z.-Y. Shih, A. P. Periasamy, P.-C. Hsu, H.-T. Chang *Appl. Catal., B* **2013**, *132- 133*, 363−369.

[43] R. Kaur, B. Pal *Appl. Catal. A: Gen.* **2015**, *491*, 28−36.

[44] R. C. Pawar, D.-H Choi, J.-S Lee, C. S. Lee *Mater. Chem. Phys.* **2015**, *151*, 167−180.

[45] G. Yin, M. Nishikawa, Y. Nosaka, N. Srinivasan, D. Atarashi, E. Sakai, M. Miyauchi *ACS Nano* **2015**, *9*, 2111−2119.

[46] Y. Zhu, X. Kong, X. Li, G. Ding, Y. Zhu, Y.-W. Li *ACS Catal.* **2014**, *4*, 3612−3620.

[47] R. V. Goncalves, R. Wojcieszak, H. Wender, C. S. B. Dias, L. L. R. Vono, D. Eberhardt, S. R. Teixeira, L. M. Rossi *ACS Appl. Mater. Interfaces* **2015**, *7*, 7987−7994.

[48] M. J. Albaladejo, F. Alonso, M. J. Gonzalez-Soria *ACS Catal.* **2015**, *5*, 3446− 3456.

[49] R. Poreddy, C. Engelbrekt, A. Riisager *Catal. Sci. Technol*. **2015**, *5*, 2467−2477.

[50] Y. Ahn, Y. Jeong, D. Lee, Y. Lee, Y *ACS Nano* **2015**, *9*, 3125−3133.

[51] S. Bhanushali, P. Ghosh, A. Ganesh, W. Cheng *Small* **2015**, *11*, 1232−1252.

[52] G. A. Somorjai, J. Y. Park *Angew. Chem., Int. Ed. Engl.* **2008**, *47*, 9212−9228.

[53] M. A. Ben Aissa, B. Tremblay, A. Andrieux-Ledier, E. Maisonhaute, N. Raouafi, A. Courty *Nanoscale* **2015**, *7*, 3189−3195.

[54] D. Tuschel *Spectroscopy* **2014**, *29*, 14.

[55] Y. Deng, A. D. Handoko, Y.a Du, S. Xi, B. S. Yeo *ACS Catal.* **2016**, *6*, 2473-2481.

[56] Y. Shen, M. Guo, X. Xia, G. Shao *Acta Mater.* **2015**, *85*, 122-131.

[57] F. Severino, J. L. Brito, J. Laine, J. L. G. Fierro, A. López Agudo *J. Catal.* **1998**, *177*, 82-95.

[58] I. Platzman, R. Brener, H. Haick, R. Tannenbaum *J. Phys. Chem. C* **2008**, *112*, 1101-1108.

[59] Y. V. Larichev, B. L. Moroz, V. I. Bukhtiyarov *Appl. Surf. Sci.* **2011**, *258*, 1541-1550.

[60] K. Grzelak, M. Trejda, J. Gurgul. *Materials* **2022**, *15*, 4877.

[61] M. C. Biesinger *Surf. Interface Anal.* **2017**, *49*, 1325-1334.

[62] A. Białas, K. Rugała, C. Czosnek, G. Mordarski, J. Gurgul *Catalysts* **2020**, *10*, 1388.

[63] J. Ghijsen, L.-H. Tjeng, J. van Elp, H. Eskes, J. Westerink, G. A. Sawatzky, M. T. Czyzyk *Phys. Rev. B* **1988**, *38*, 11322.

[64] NIST, XPS. "Database https://srdata. nist. gov/xps/(accessed Apr 8, 2020). https://doi. org/10.18434."

[65] M. C. Biesinger, B. P. Payne, A. P. Grosvenor, L. W.M. Lau, A. R. Gerson, R. St.C. Smart *Appl. Surf. Sci.* **2010**, *257*, 887-898.

[66] Ch.-K. Wu, M. Yin, S. O'Brien, J. T. Koberstein *Chem. Mater.* **2006**, *18*, 6054-6058.

[67] C. C. Chusuei, M. A. Brookshier, D. W. Goodman *Langmuir* **1999**, *15*, 2806-2808.

[68] J. Timoshenko, D. Lu, Y. Lin, A. I. Frenkel *J. Phys. Chem. Lett.* **2017**, *8*, 5091-5098.

[69] D. Cabaret, A. Bordage, A. Juhin, M. Arfaoui, E. Gaudry *Phys. Chem. Chem. Phys.* **2010**, *12*, 5619-5633.

[70] R. Yang, D. J. Morris, T. Higaki, M. J. Ward, R. Jin, P. Zhang *ACS omega* **2018**, *3*, 14981-14985.

[71] H. Huang, Y. Xu, G. Luo, Z. Xie, W. Ming *Nanomaterials* **2022**, *12*, 1524.

[72] M. Feng, X. Z. Jiang, W. Zeng, K. H. Luo, P. Hellier *Fuel* **2019**, *235*, 515-521.

[73] J. Wang, G.-Ch. Wang *J. Phys. Chem. C* **2018**, *122*, 17338-17346.

[74] M. Kański, S. Hrabar, A. C. T. van Duin, Z. Postawa *J. Phys. Chem. Lett.* **2022**, *13*, 628-633.

[75] T. Cheng, H. Xiao, W. A. Goddard *J. Am. Chem. Soc.* **2017**, *139*, 11642-11645.

[76] P. Ferrin, D. Simonetti, S. Kandoi, E. Kunkes, J. A. Dumesic, J. K. Nørskov, M. Mavrikakis *J. Am. Chem. Soc.* **2009**, *131*, 5809-5815.

[77] M. K. Debe *Nature* **2012**, *486*, 43-51.

[78] S. Duran, M. Elmaalouf, M. Odziomek, J.-Y. Piquemal, M. Faustini, M. Giraud, J. Peron, C. Tard. *ChemElectroChem* **2021**, *8*, 3519-3524.

[79] M. Dupont, A. F. Hollenkamp, S.W. Donne *Electrochim. Acta* **2013**, *104*, 140-147.

[80] X. Wang, J. C. Hanson, A. I. Frenkel, J.-Y. Kim, J. A. Rodriguez *J. Phys. Chem. B* **2004**, *108*, 13667-13673.

[81] A. Kowal, M. Li, M. Shao, K. Sasaki, M. B. Vukmirovic, J. Zhang, N. S. Marinkovic, P. Liu, A. I. Frenkel, R. R. Adzic *Nat. Mater.* **2009**, *8*, 325-330.

[82] S. R. Khan, S. Kanwal, M. Hashaam, S. Jamil, B. Ullah, and M. R. S. A. Janjua *Mater. Res. Express* **2020**, *7*, 025036.

[83] X. Wang, J. C. Hanson, A. I. Frenkel, J.-Y. Kim, J. A. Rodriguez *J. Phys. Chem. B* **2004**, *108*, 13667-13673.

[84] D. B. Rorabacher *Chem. Rev.* **2004**, *104*, 651-698.

[85] A. Prajapati, B. A. Collins, J. D. Goodpaster, M. R. Singh *Proc. Natl. Acad. Sci. U.S.A.* **2021**, *118*, e2023233118.

[86] S. Najafishirtari, K. F. Ortega, M. Douthwaite, S. Pattisson, G. J. Hutchings, C. J. Bondue, K. Tschulik, D. Waffel, B. Peng, M. Deitermann, G. W. Busser, M. Muhler, M. Behrens *Chem. Eur. J.* **2021**, *27*, 16809-16833.

[87] B. Ravel, M. Newville *J. Synchrotron Radiat.* **2005**, *12*, 537-541.

[88] W. Zhu, H. Gong, Y. Han, M. Zhang, A. C.T. Van Duin *J. Phys. Chem. C* **2020**, *124*, 12512-12520.

[89] R. Rüger, M. Franchini, T. Trnka, A. Yakovlev, E. van Lenthe, P. Philipsen, T. van Vuren, B. Klumpers, T. Soini, AMS 2022.1, SCM, Theoretical Chemistry, Vrije Universiteit, Amsterdam, The Netherlands, http://www.scm.com.

[90] Ch. Ashraf, A. C.T. Van Duin *J. Phys. Chem. A* **2017**, *121*, 1051-1068.

[91] A. C.T. Van Duin, S. Dasgupta, F. Lorant, W. A. Goddard *J. Phys. Chem. A* **2001**, *105*, 9396-9409.

[92] K. D. Nielson, A. C.T. Van Duin, J. Oxgaard, W.-Q. Deng, W. A. Goddard *J. Phys. Chem. A* **2005**, *109*, 493-499.

[93] A. C.T. Van Duin, V. S. Bryantsev, M. S. Diallo, W. A. Goddard, O. Rahaman, D. J. Doren, D.Raymand, K. Hermansson *J. Phys. Chem. A* **2010**, *114*, 9507-9514.

[94] T. P. Senftle, S. Hong, M. M. Islam, S. B. Kylasa, Y. Zheng, Y. K. Shin, C. Junkermeier, R. Engel-Herbert, M. J Janik, H. M. Aktulga, T. Verstraelen, A. Grama, A. C. T. van Duin *Npj Comput. Mater.* **2016**, *2*, 1-14.

[95] K. Chenoweth, A. C.T. Van Duin, W. A. Goddard *J. Phys. Chem. A* **2008**, *112*, 1040-1053.

[96] M. Feng, X. Z. Jiang, K. H. Luo *Proc. Combust. Inst.* **2019**, *37*, 5473-5480.

[97] Q. Mao, A. C. T. Van Duin, K. H. Luo *Carbon* **2017**, *121*, 380-388.

[98] M. Döntgen, M.-D. Przybylski-Freund, L. C. Kröger, W. A. Kopp, A. E. Ismail, K. Leonhard *J. Chem. Theory Comput.* **2015**, *11*, 2517-2524.

[99] W. Humphrey, A. Dalke, K. Schulten *J. Mol. Graph.* **1996**, *14*, 33-38.

[100] P. Giannozzi, O. Andreussi, T. Brumme, O. Bunau, M. Buongiorno Nardelli, M. Calandra, R. Car, C. Cavazzoni, D. Ceresoli, M. Cococcioni, N. Colonna, I. Carnimeo, A. Dal Corso, S. de Gironcoli, P. Delugas, R. A. DiStasio Jr, A. Ferretti, A. Floris, G. Fratesi, G. Fugallo, R. Gebauer, U. Gerstmann, F. Giustino, T. Gorni, J Jia, M. Kawamura, H.-Y. Ko, A. Kokalj, E. Küçükbenli, M .Lazzeri, M. Marsili, N. Marzari, F. Mauri, N. L. Nguyen, H.-V. Nguyen, A. Otero-de-la-Roza, L. Paulatto, S. Poncé, D. Rocca, R. Sabatini, B. Santra, M. Schlipf, A. P. Seitsonen, A. Smogunov, I. Timrov, T. Thonhauser, P. Umari, N. Vast, X. Wu, S. Baroni *J. Phys. Condens. Matter.* **2017**, *29*, 465901.

[101] P. Giannozzi, S. Baroni, N. Bonini, M. Calandra, R. Car, C. Cavazzoni, D. Ceresoli, G. L. Chiarotti, M. Cococcioni, I. Dabo, A. Dal Corso, S. Fabris, G. Fratesi, S. de Gironcoli, R. Gebauer, U. Gerstmann, C. Gougoussis, A. Kokalj, M. Lazzeri, L. Martin-Samos, N. Marzari, F. Mauri, R. Mazzarello, S. Paolini, A. Pasquarello, L. Paulatto, C. Sbraccia, S. Scandolo, G. Sclauzero, A. P. Seitsonen, A. Smogunov, P. Umari, R. M. Wentzcovitch *J. Phys. Condens. Matter.* **2009**, *21*, 395502.

[102] P. Giannozzi, O. Baseggio, P. Bonfà, D. Brunato, R. Car, I. Carnimeo, C. Cavazzoni, S. de Gironcoli, P. Delugas, F. Ferrari Ruffino, A. Ferretti, N. Marzari, I. Timrov, A. Urru, S. Baroni *J. Chem. Phys.* **2020**, *152*, 154105.

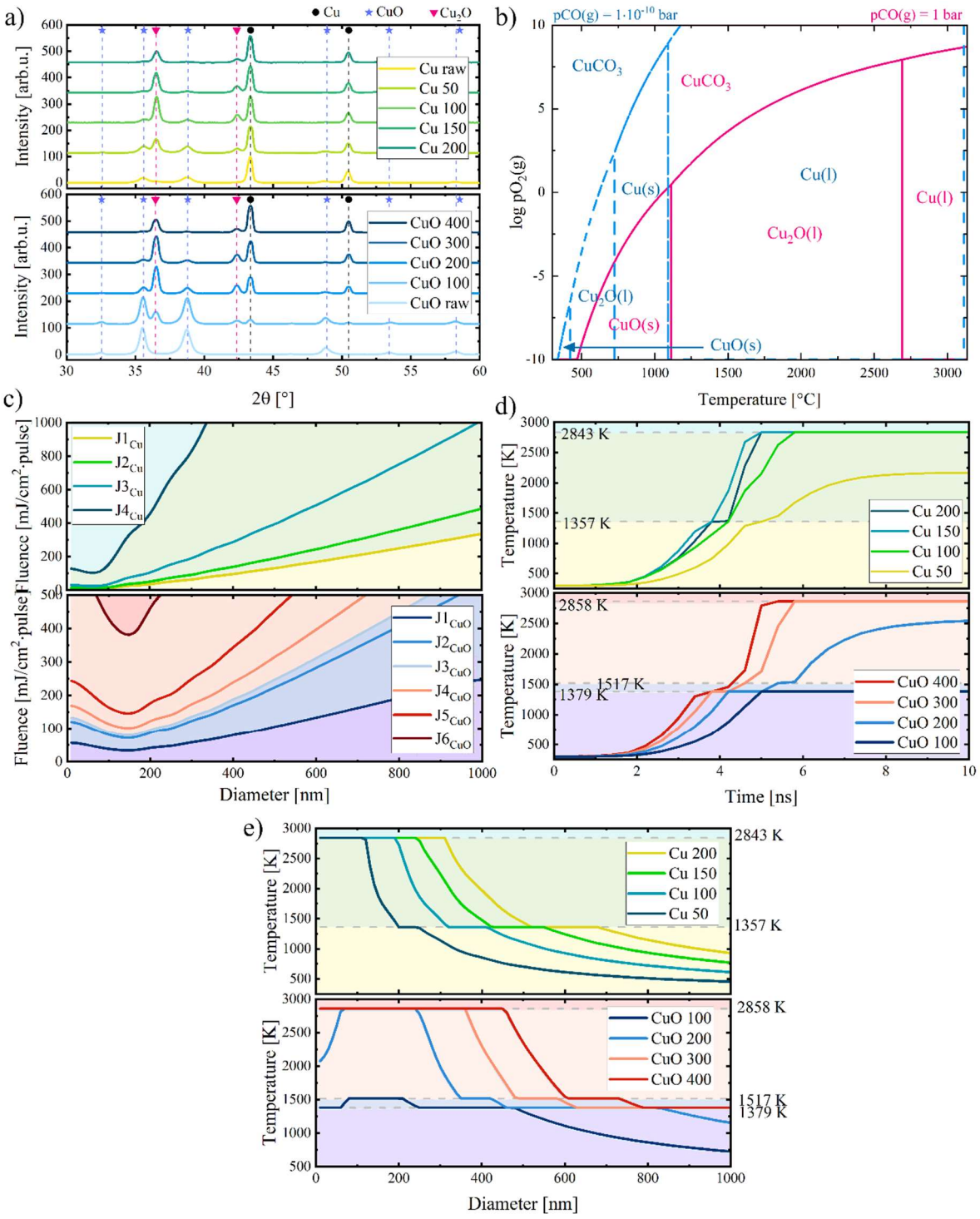
a)
Cu
CuO
Cu2O
Intensity [arb.u.]
Cu raw
Cu 50
Cu 100
Cu 150
Cu 200
CuO 400
CuO 300
CuO 200
CuO 100
CuO raw
2θ [°]
b)
pCO(g) – 1·10-10 bar
pCO(g) = 1 bar
CuCO3
CuCO3
Cu(s)
Cu(l)
Cu(l)
Cu2O(l)
Cu2O(l)
CuO(s)
CuO(s)
log pO2(g)
Temperature [°C]
c)
J1Cu
J2Cu
J3Cu
J4Cu
Fluence [mJ/cm2·pulse]
J1CuO
J2CuO
J3CuO
J4CuO
J5CuO
J6CuO
Diameter [nm]
d)
2843 K
1357 K
Cu 200
Cu 150
Cu 100
Cu 50
Temperature [K]
2858 K
1517 K
1379 K
CuO 400
CuO 300
CuO 200
CuO 100
Time [ns]
e)
Cu 200
Cu 150
Cu 100
Cu 50
2843 K
1357 K
CuO 100
CuO 200
CuO 300
CuO 400
2858 K
1517 K
1379 K
Temperature [K]
Diameter [nm]

Figure 1. Phase analysis and temperature evolution in the system. (a) XRD patterns of Cu-ethanol and CuO-ethanol samples containing Cu, CuO and Cu_2O phases. (b) $Log\, P_{O_2} - T$ plot at $P_{CO} = 1\ and\ 1 \times 10^{-10}$ bar calculated using HSC Chemistry software for the Cu-O-C system. (c) Plot of laser fluence versus diameter (J-D) of Cu-ethanol and CuO-ethanol. To display phase diagrams with the functionality of laser/suspension parameters, the reaction pathways of Cu and CuO phases were recorded by calculating the temperature dependence of enthalpy and Gibbs free energy of the phases (Table S2 and Figure S2). Consequently, $J\sigma_{abs}^{\lambda}(d) = m_p \Delta H$ was solved numerically to represent the laser fluence (J) required for all possible transitions as a function of particle sizes. (d) Temperature profile of Cu-ethanol and CuO-ethanol systems showing how the temperature of a sphere changes during absorption of a laser pulse. The temperature profile of the particles was calculated numerically using the 4th order Rung-Kutta solution of $\frac{dE}{dt} = \frac{dE_{abs}}{dt} - \frac{dq}{dt}$ when both energy absorption and heat release are considered, simultaneously. These curves were plotted for the Cu sphere with a diameter of 200 nm and the CuO sphere with a diameter of 250 nm, which were selected on the basis of the average agglomerate size of their stable suspension in ethanol (Figure S22). (e) Maximum temperature of particles as a function of size for Cu-ethanol and CuO-ethanol samples. The dashed lines show the transition temperatures. The initial size distribution of agglomerates in the suspension is believed to be responsible for the multiphase crystallization leading to the synthesis of Cu-CuO-Cu_2O heterostructures. For the diagrams in (c), (d), and (e), the yellow, green, and turquoise fill colors indicate solid, liquid, and gaseous Cu, respectively, for Cu-based diagrams. For CuO-based diagrams, the purple, blue, orange and red colors indicate solid CuO, solid Cu_2O, liquid Cu_2O and gaseous Cu, respectively.

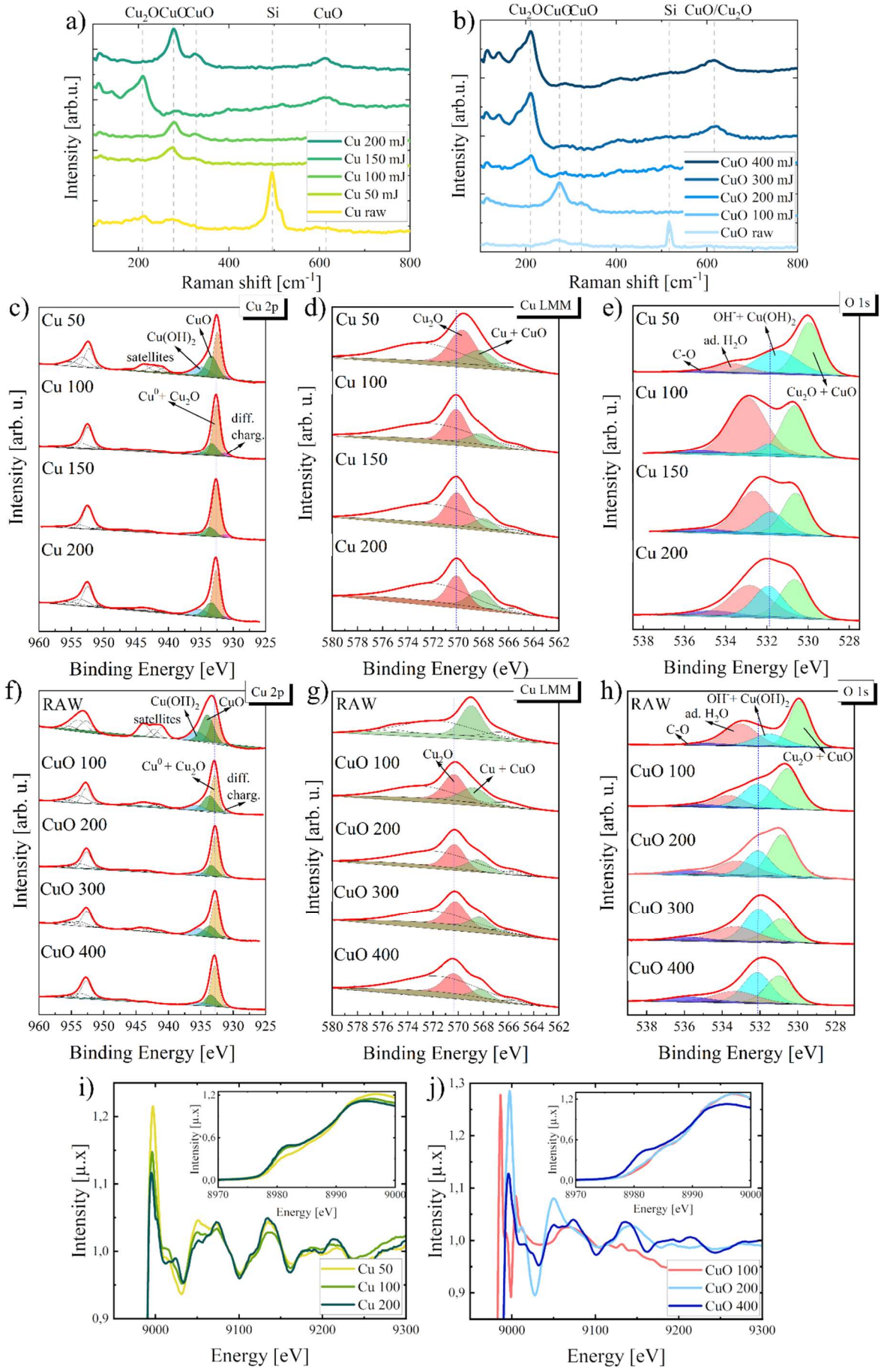
a)
Cu2O CuO CuO
Si
CuO
Intensity [arb.u.]
Cu 200 mJ
Cu 150 mJ
Cu 100 mJ
Cu 50 mJ
Cu raw
Raman shift [cm-1]
b)
Cu2O CuO CuO
Si CuO/Cu2O
Intensity [arb.u.]
CuO 400 mJ
CuO 300 mJ
CuO 200 mJ
CuO 100 mJ
CuO raw
Raman shift [cm-1]
c)
Cu 2p
Cu 50
CuO
Cu(OH)2
satellites
Cu 100
Cu0 + Cu2O
diff. charg.
Cu 150
Cu 200
Intensity [arb. u.]
Binding Energy [eV]
d)
Cu LMM
Cu 50
Cu2O
Cu + CuO
Cu 100
Cu 150
Cu 200
Intensity [arb. u.]
Binding Energy (eV)
e)
O 1s
Cu 50
OH- + Cu(OH)2
ad. H2O
C-O
Cu 100
Cu2O + CuO
Cu 150
Cu 200
Intensity [arb. u.]
Binding Energy [eV]
f)
Cu 2p
RAW
Cu(OH)2
CuO
satellites
CuO 100
Cu0 + Cu2O
diff. charg.
CuO 200
CuO 300
CuO 400
Intensity [arb. u.]
Binding Energy [eV]
g)
Cu LMM
RAW
CuO 100
Cu2O
Cu + CuO
CuO 200
CuO 300
CuO 400
Intensity [arb. u.]
Binding Energy [eV]
h)
O 1s
RAW
OH- + Cu(OH)2
ad. H2O
C-O
CuO 100
Cu2O + CuO
CuO 200
CuO 300
CuO 400
Intensity [arb. u.]
Binding Energy [eV]
i)
Intensity [μ.x]
Energy [eV]
Cu 50
Cu 100
Cu 200
j)
Intensity [μ.x]
Energy [eV]
CuO 100
CuO 200
CuO 400

Figure 2. Static oxidation evaluation in the system. Raman spectra of (a) Cu-ethanol and (b) CuO-ethanol samples. Each sample was analyzed with more than 5 laser foci of Raman spectroscopy, and the data presented here are those obtained with the maximum repetition (Figure S16). Among 9 optical phonon modes of CuO with C_{2h}^{6} space group and 15 modes of Cu_2O with O_h^4 space group, 4 vibrational modes were observed in the Raman spectra of the samples, shown with dashed lines. XPS analysis of (c) Cu 2p, (d) Cu LMM, and (e) O 1s spectra for Cu-ethanol system. XPS analysis of (f) Cu 2p, (g) Cu LMM, and (h) O 1s spectra for CuO-ethanol system. The Cu 2p, Cu LMM, and O 1s spectra were fitted with 4, 2, and 4 spin-orbit doublets, respectively. The details of the quantitative analysis derived from XPS curves were presented in supplementary part c. Normalized extended X-ray absorption fine structure (EXAFS) and X-ray absorption near edge structure (XANES) for Cu K-edge spectra of (i) Cu-ethanol and (j) CuO-ethanol samples. All samples were analyzed 3 times and the average spectrum was reproduced here. Analysis of the Cu foil reference sample was performed before each measurement to meet calibration criteria. The changes in the oxidation state of the composite powders are shown in these curves. The detailed X-ray absorption spectroscopy (XAS) analysis is described in supplementary part d.

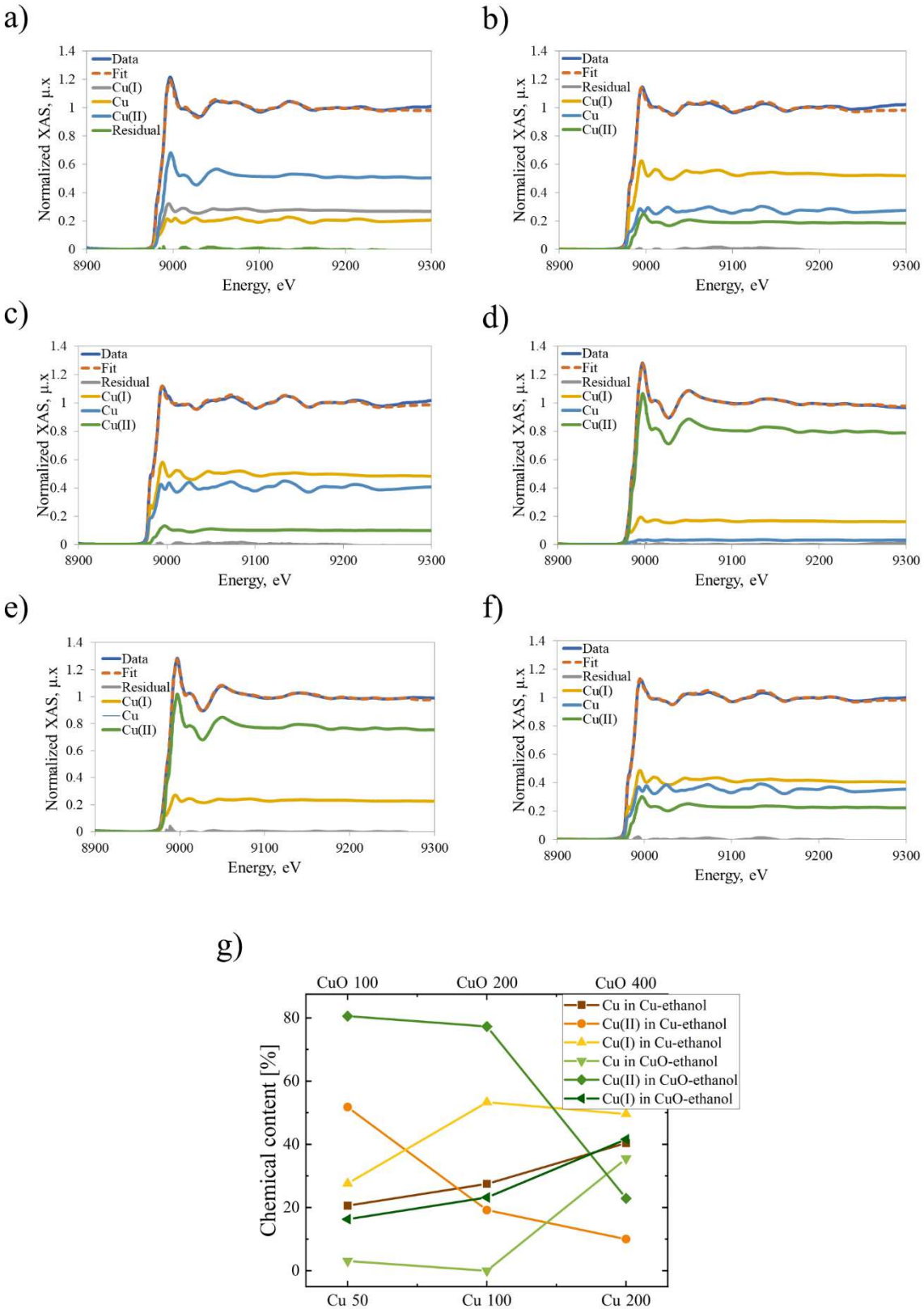
a)
b)
c)
d)
e)
f)
Data
Fit
Residual
Cu(I)
Cu
Cu(II)
Normalized XAS, μ.x
Energy, eV
g)
CuO 100
CuO 200
CuO 400
Chemical content [%]
Cu 50
Cu 100
Cu 200
Cu in Cu-ethanol
Cu(II) in Cu-ethanol
Cu(I) in Cu-ethanol
Cu in CuO-ethanol
Cu(II) in CuO-ethanol
Cu(I) in CuO-ethanol

Figure 3. Quantitative analysis of EXAFS spectra. Linear combination fitting (LCF) of normalized EXAFS spectra of (a) Cu50, (b) Cu100, (c) Cu200, (d) CuO100, (e) CuO200, and (f) CuO400 samples using copper foil, CuO Merck, and Cu_2O Merck references. The amount of residual for all fitting curves is less than 1%. (g) Quantitative phase analysis of samples derived from LCF of EXAFS spectra. Although the changes have been shown for samples irradiated by three different laser fluences, the exponential and logarithmic trend of increase/decrease of each phase is obvious which have been connected to the physical/chemical phase formation during PLIS.

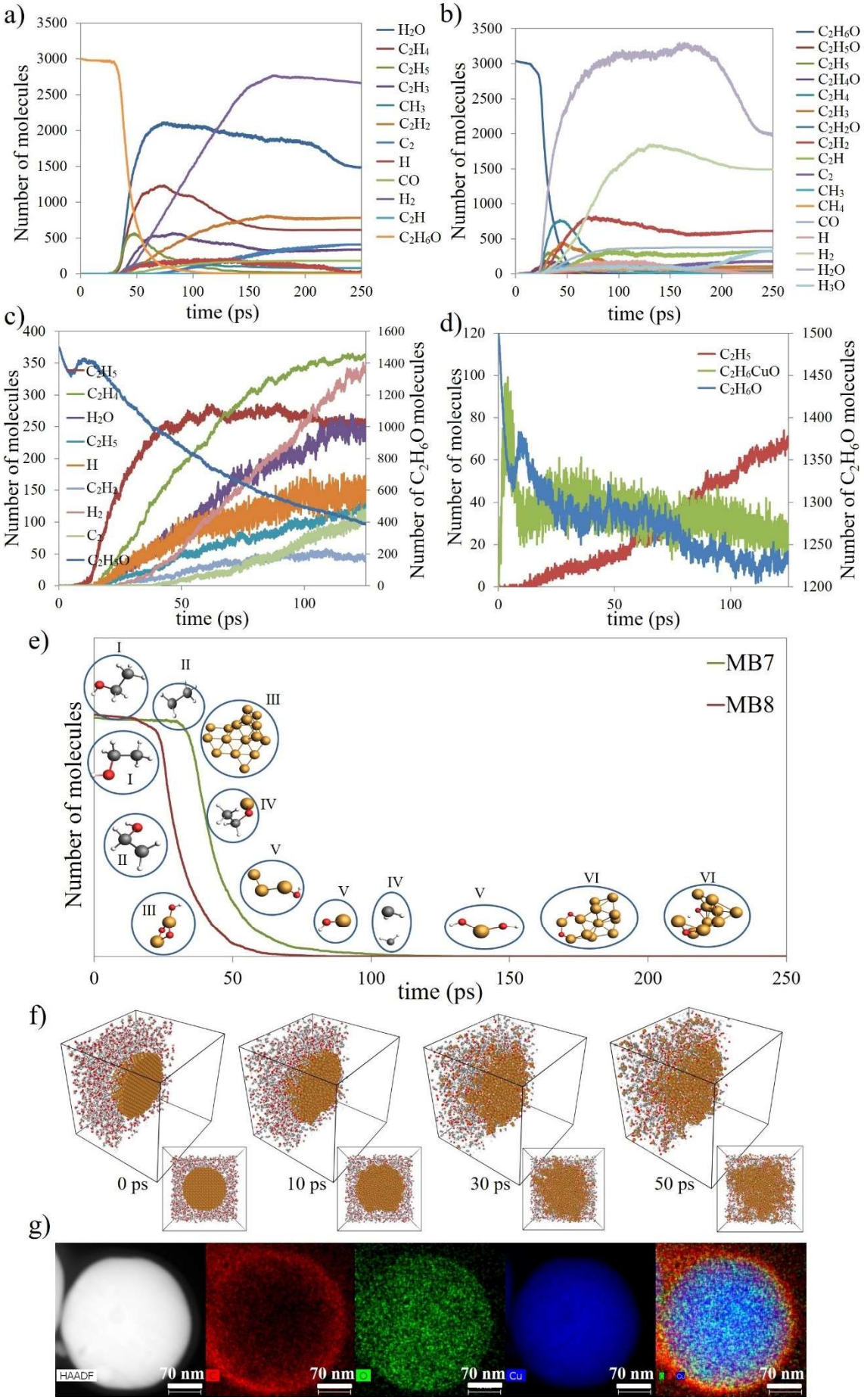
a)
Number of molecules
time (ps)
H_2O
C_2H_4
C_2H_5
C_2H_3
CH_3
C_2H_2
C_2
H
CO
H_2
C_2H
C_2H_6O
b)
Number of molecules
time (ps)
C_2H_6O
C_2H_5O
C_2H_5
C_2H_4O
C_2H_4
C_2H_3
C_2H_2O
C_2H_2
C_2H
C_2
CH_3
CH_4
CO
H
H_2
H_2O
H_3O
c)
Number of molecules
Number of C_2H_6O molecules
time (ps)
C_2H_5
C_2H_4
H_2O
C_2H_5
H
C_2H_2
H_2
C_2
C_2H_5O
d)
Number of molecules
Number of C_2H_6O molecules
time (ps)
C_2H_5
C_2H_6CuO
C_2H_6O
e)
Number of molecules
time (ps)
MB7
MB8
I
II
III
IV
V
VI
f)
0 ps
10 ps
30 ps
50 ps
g)
HAADF
70 nm
O
Cu
Cl

Figure 4. Reactive bond force field molecular dynamics simulations (RBFF-MD). Solvent decomposition and formation of new species from ethanol calculated using RBFF-MD for (a) Cu-ethanol system according to RB1 model at 2843 K, and (b) CuO-ethanol system according to RB2 model at 2858 K. The maximum temperature for each system was chosen based on the data shown in Figure 1e. Solvent decomposition and formation of new species calculated with RBFF-MD for the Cu-ethanol system at a sphere temperature of 2843 K (c) with the RB5 model at a solvent temperature of 1000 K, and (d) with the RB6 model at a solvent temperature of 298 K. (e) Timeline of new species formation on the decomposition curves of ethanol for the Cu-ethanol and CuO-ethanol systems according to models RB7 and RB8. The species shown here were selected from thousands of new species according to their higher repetition to show the mechanism of bond breaking/formation in the systems. The evolution of the mechanism for Cu-ethanol is illustrated by (I) ethanol absorption, (II) hydroxyl cleavage, (III) formation of Cu clusters, (IV) surface oxidation, (V) further decomposition of the solvent, and (VI) net oxidation. Also shown is (I) the absorption of ethanol, (II) hydrogen splitting from ethanol, and (III) formation of hydrogenated copper oxide for the CuO-ethanol system. The main difference between bond breaking mechanisms in Cu-ethanol and CuO-ethanol systems is that copper absorbs oxygen from ethanol ($2Cu + \frac{1}{2}O_2 = Cu_2O$), while ethanol absorbs oxygen from copper oxide ($C_2H_5OH + 2O_2 = 2CO_2 + 3H_2O$), both for oxidation purposes. These data were collected using the ChemTraYzer module of the AMS software based on a statistical analysis of all time steps of the simulations. (F) 3D perspective and front snapshots of the sliced box of the MB1 model during RBFF-MD simulation showing diffusion of species during the bond breaking/formation process. The diffusion of oxygen and hydrogen deep into the sphere and the remaining carbon compounds at the surface layer was confirmed by the EDX analysis results. (g) HAADF-EDX Analysis of a Cu_2O particle synthesized by laser irradiation of a Cu-ethanol suspension at a laser fluence of 150 mJ/cm^2.pulse (Cu150 sample). The accumulation of carbon on the surface is clearly visible.

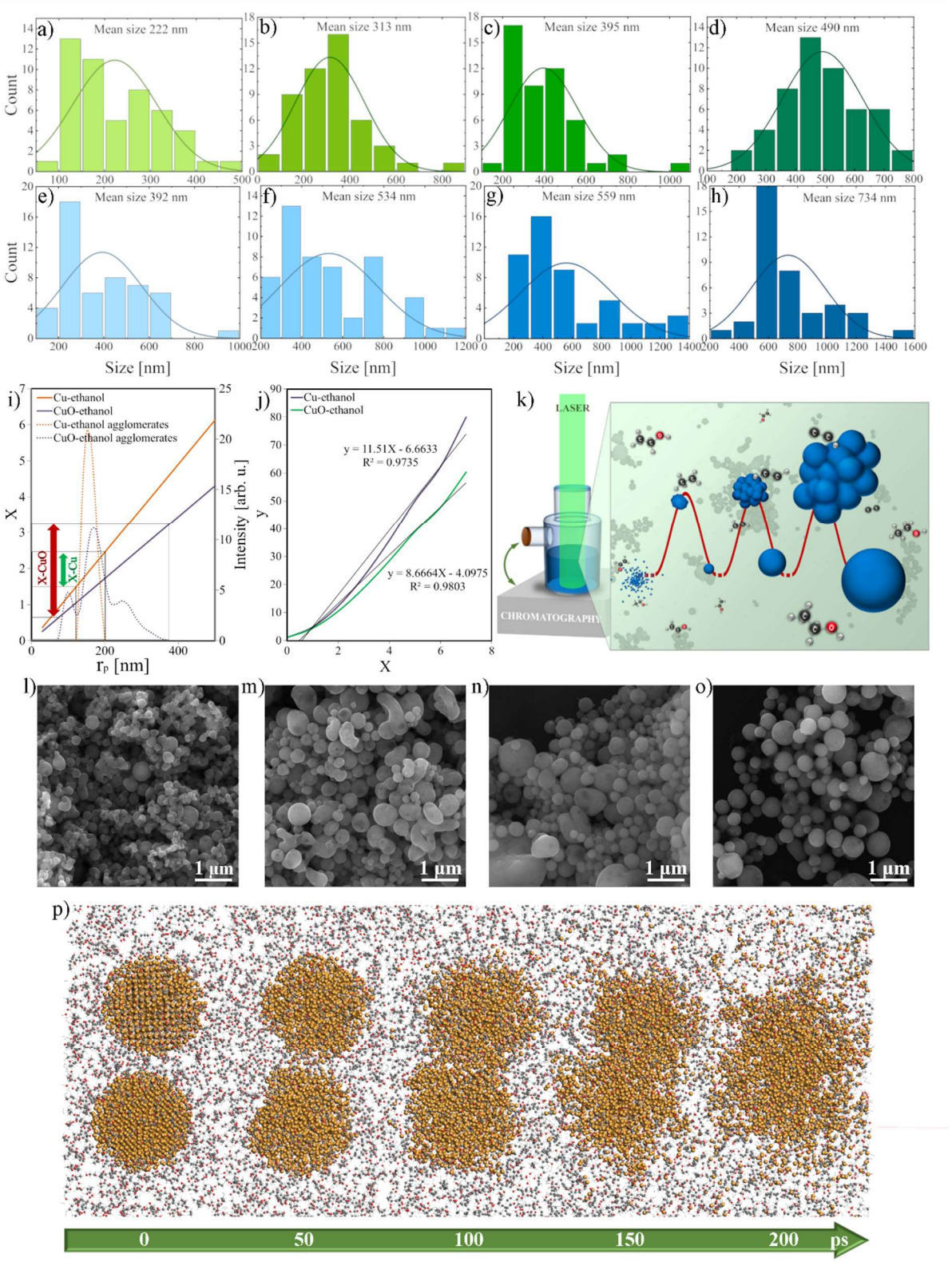
a) Mean size 222 nm
b) Mean size 313 nm
c) Mean size 395 nm
d) Mean size 490 nm
e) Mean size 392 nm
f) Mean size 534 nm
g) Mean size 559 nm
h) Mean size 734 nm
Count
Size [nm]
i)
Cu-ethanol
CuO-ethanol
Cu-ethanol agglomerates
CuO-ethanol agglomerates
X-CuO
X-Cu
X
Intensity [arb. u.]
rp [nm]
j)
Cu-ethanol
CuO-ethanol
y = 11.51X - 6.6633
R² = 0.9735
y = 8.6664X - 4.0975
R² = 0.9803
y
X
k)
LASER
CHROMATOGRAPHY
l)
m)
n)
o)
1 µm
p)
0
50
100
150
200
ps

Figure 5. Particle growth during PLIS process. Particle size distribution of (a-d) Cu-ethanol and (e-h) CuO-ethanol samples measured from analysis of 50 particles in SEM images using ImageJ software. The increasing trend of particle size with laser fluence intensity is clearly visible in both groups of samples. (i) Probability of the probe as a function of particle size for both Cu-ethanol and CuO-ethanol systems. According to the initial size distribution of copper and copper oxide agglomerates shown by dashed lines (Figure S21), the probability of probe changes in the range of 1.5-2.5 for Cu-ethanol and 0.7-3.2 for CuO-ethanol samples. (j) y-X curve for Cu-ethanol and CuO-ethanol systems. $y = {}^{r_p}/_{r_{p_0}}$ as growth ratio shows that the particles in the Cu-ethanol system grow at a higher rate than in the CuO-ethanol system. (k) Schematic illustrating the growth mechanism of particles formed not only by physical phase transitions but also by interfacial reactions with the dissociated ethanol. The formation of smaller hydrocarbons in the latter pulse probe shows greater dissociation of ethanol to H_2, C_2, and CO in the absence of sufficient oxygen. SEM images of (l) Cu50, (m) Cu100, (n) Cu150, and (o) Cu200 samples showing the formation of irregular shapes with necking zones at lower laser fluences and also soundless spherical particles mainly at higher laser fluences. (p) Snapshots of the front view of the MB9 model showing the formation of necking zone between two particles during RBMD simulation.

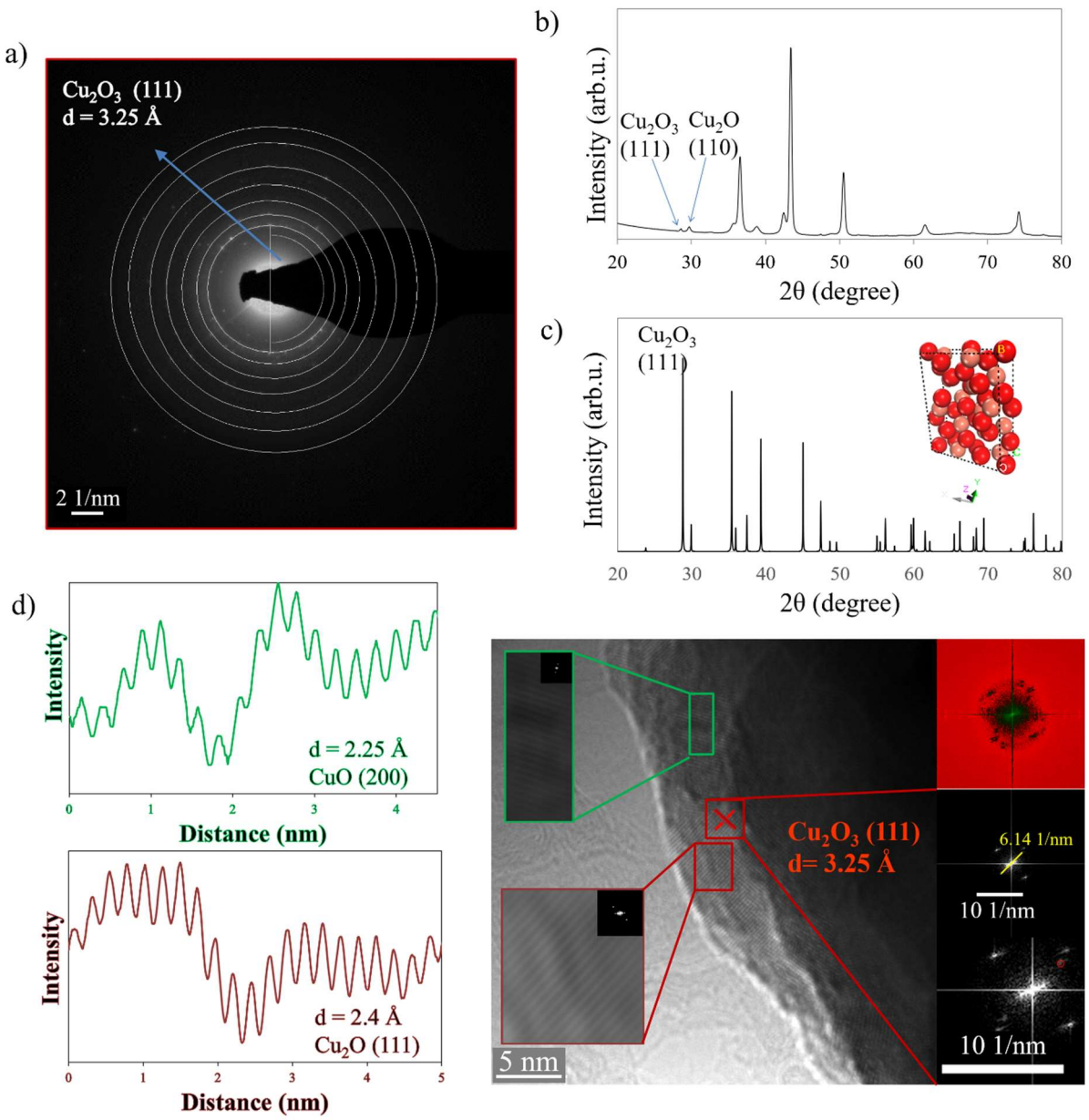
a)
Cu_2O_3 (111)
d = 3.25 Å
2 1/nm
b)
Intensity (arb.u.)
Cu_2O_3 (111)
Cu_2O (110)
20 30 40 50 60 70 80
2θ (degree)
c)
Cu_2O_3 (111)
Intensity (arb.u.)
20 30 40 50 60 70 80
2θ (degree)
d)
Intensity
d = 2.25 Å
CuO (200)
0 1 2 3 4
Distance (nm)
Intensity
d = 2.4 Å
Cu_2O (111)
0 1 2 3 4 5
Distance (nm)
Cu_2O_3 (111)
d= 3.25 Å
6.14 1/nm
10 1/nm
10 1/nm
5 nm

Figure 6. Analysis of the possibility for Cu_2O_3 formation. (a) SAED pattern of a Cu200 particle showing the traces of Cu_2O_3 phase in a multiphase particle containing CuO and Cu_2O. (b) High-resolution XRD pattern of Cu200 sample analyzed at a slow rate of 0.05°/min. It shows a characteristic peak associated with the Cu_2O_3 (111) plane at $2\theta = 27.5°$. (c) Calculated XRD pattern of a relaxed orthogonal Cu_2O_3 unit cell using DFT. (d) FFT analysis of a Cu200 particle showing the crystallization of Cu_2O_3 at the interface of the CuO and Cu_2O oxides based on the calculation of the d-spacing. The enrichment of oxygen during the transition between stable copper oxides (I & II) was considered to be the reason for the crystallization of copper (III) in their interface.

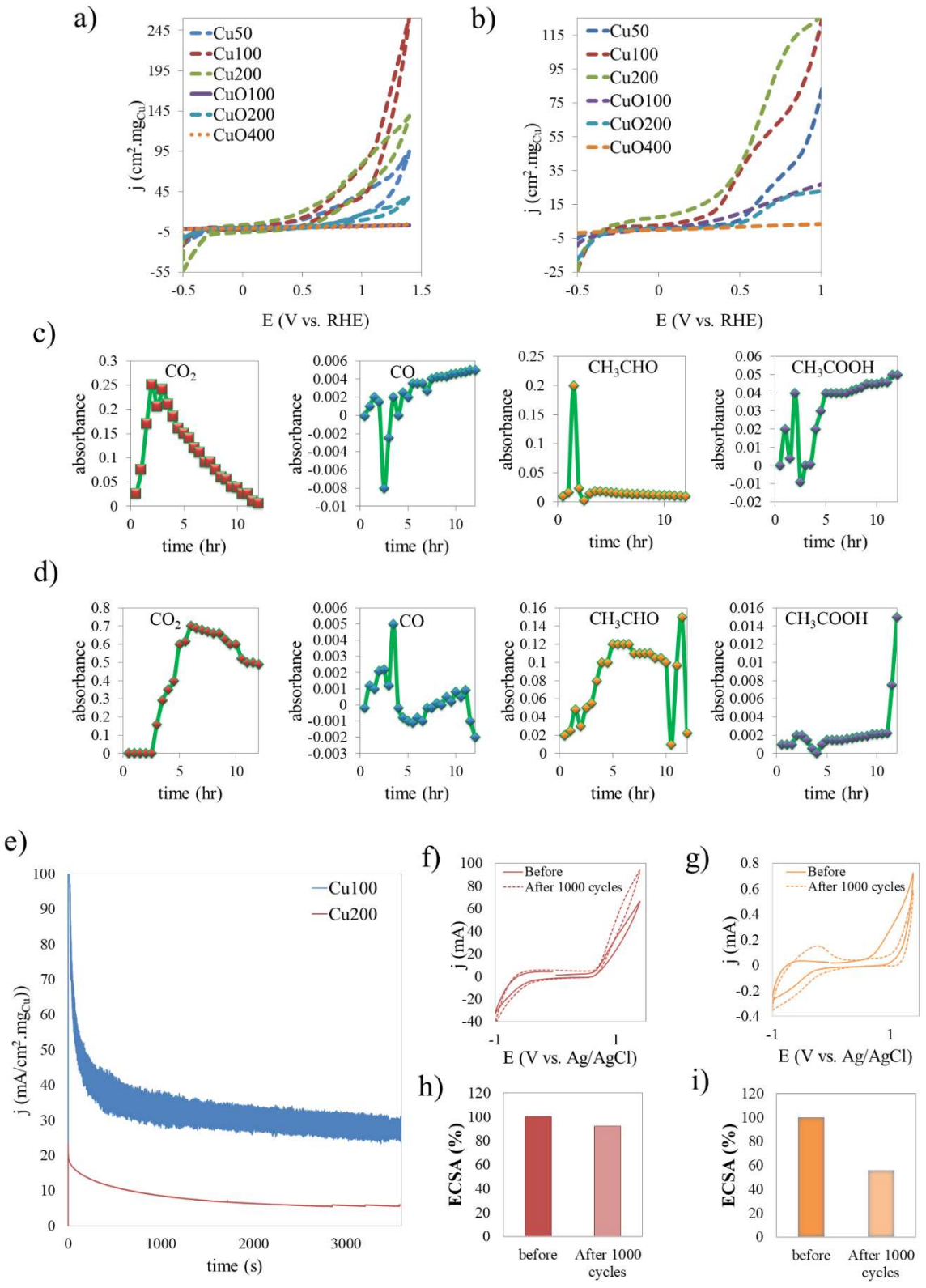
a)
Cu50
Cu100
Cu200
CuO100
CuO200
CuO400
j (cm².mgCu)
E (V vs. RHE)
b)
Cu50
Cu100
Cu200
CuO100
CuO200
CuO400
j (cm².mgCu)
E (V vs. RHE)
c)
CO2
CO
CH3CHO
CH3COOH
absorbance
time (hr)
d)
CO2
CO
CH3CHO
CH3COOH
absorbance
time (hr)
e)
Cu100
Cu200
j (mA/cm².mgCu))
time (s)
f)
Before
After 1000 cycles
j (mA)
E (V vs. Ag/AgCl)
g)
Before
After 1000 cycles
j (mA)
E (V vs. Ag/AgCl)
h)
ECSA (%)
before
After 1000 cycles
i)
ECSA (%)
before
After 1000 cycles

Figure 7. (a) Cyclic voltammetry of Cu50/C, Cu100/C, Cu200/C, CuO100/C, CuO200/C and CuO400/C electrocatalysts in 0.1 M NaOH, with a sweep rate of 50 mV/s; (b) EOR forward scan of the Cu50/C, Cu100/C, Cu200/C, CuO100/C, CuO200/C and CuO400/C catalysts. All curves were recorded in 0.1 M NaOH + 0.5 M C2H5OH solution at a scan rate of 50 mV/s at room temperature. Differences in the absorbance of peaks originating from CO_2, CO, CH_3CHO, and CH_3COOH species were observed during 12 h of EOR for (c) Cu200/C and (d) Cu100/C catalysts. The dynamics of ethanol oxidation mostly shows the dominant mechanism of complete oxidation leading to enormous CO_2 production. The optimum catalyst, i.e. Cu100/C, retains its oxidation potential for 12 hours, which is not the case at all with Cu200/C. After 12 hours, Cu100/C can still be used as a catalyst for complete oxidation of ethanol, while Cu200/C is a better choice for partial oxidation. (e) Current–time curves recorded at 0.5 vs. Ag/AgCl for 3,600 s in 0.1 M NaOH + 0.5 M ethanol solution. Cyclic voltammogram curves of the (f) Cu100/C and (g) Cu200/C catalysts before and after 10000 potential cycles. The graphs showing the decrease of ECSA (%) for (h) Cu100/C and (i) Cu200/C.

Table 1. Transition temperature, enthalpy, and laser fluence required for the reaction pathways of Cu and CuO phases

No.	Heating regime	Reaction	Initial Temperature (K)	Final Temperature (K)	ΔH(kJ/mole)
Cu					
$J1_{Cu}$	Heating of solid Cu	Cu (s) + hυ → Cu (s)	T_0/ 298	T_m/ 1357	29.642
$J2_{Cu}$	Cu melting	Cu (s) + hυ → Cu (l)	T_m/ 1357	T_m/ 1357	13.264
$J3_{Cu}$	Heating liquid Cu	Cu (l) + hυ → Cu (l)	T_m/ 1357	T_b/ 2843	46.636
$J4_{Cu}$	Cu boiling	Cu (l) + hυ → Cu (g)	T_b/ 2843	T_b/ 2843	300.150
CuO					
$J1_{CuO}$	Heating of solid CuO	CuO (s) + hυ → CuO (s)	T_0/ 298	$T_{CuO(s)\rightarrow Cu_2O(s)}$/1379	57.073
$J2_{CuO}$	CuO decomposition to solid Cu_2O	4CuO (s) + hυ → $2Cu_2O$ (s) + O_2 (g)	$T_{CuO(s)\rightarrow Cu_2O(s)}$/1379	$T_{CuO(s)\rightarrow Cu_2O(s)}$/1379	63.881
$J3_{CuO}$	Heating of solid Cu_2O	Cu_2O (s) + hυ → $2Cu_2O$ (s)	$T_{CuO(s)\rightarrow Cu_2O(s)}$/1379	T_m/ 1517	12.378
$J4_{CuO}$	Cu_2O melting	Cu_2O (s) + hυ → Cu_2O (l)	T_m/ 1517	T_m/ 1517	65.600
$J5_{CuO}$	Heating of liquid Cu_2O	Cu_2O (l) + hυ → Cu_2O (l)	T_m/ 1517	$T_{Cu_2O(l)\rightarrow Cu(g)}$/2858	133.965
$J6_{CuO}$	Cu_2O decomposition to gaseous Cu	$2Cu_2O$ (l) + hυ → 4Cu (g) + O_2 (g)	$T_{Cu_2O(l)\rightarrow Cu(g)}$/2858	$T_{Cu_2O(l)\rightarrow Cu(g)}$/2858	706.888

Table 2. The BE values (eV) and relative areas of the components (%) of Cu $2p_{3/2}$, Cu LMM, and O 1s peaks for Cu-ethanol samples

Core excitation	Doublet No.	Cu50		Cu100		Cu150		Cu200	
		BE (eV)	Area (%)	BE (eV)	Area (%)	BE (eV)	Area (%)	BE (eV)	Area (%)
Cu $2p_{3/2}$	1	931.2	4.0	931.3	4.9	931.2	4.7	931.2	3.5
	2	932.5	42.3	932.6	63.2	932.6	70.9	932.6	52.1
	3	933.4	33.3	933.3	23.5	933.6	18.3	933.4	27.3
	4	935.0	20.4	935.4	8.4	936.3	6.1	935.2	17.1
Cu LMM	1	568.3	32.2	568.2	27.7	567.9	20.6	568.3	42.0
	2	569.7	67.8	570.2	72.3	570.1	79.4	570.1	58.0
O 1s	1	529.9	50.1	530.6	36.0	530.6	32.2	530.7	20.5
	2	531.5	36.9	531.9	5.5	531.8	18.7	531.9	51.3
	3	533.7	11.0	533.0	55.6	532.6	44.9	532.8	24.0
	4	535.1	2.0	535.4	2.9	535.1	4.2	534.6	4.2

Table 3. The BE values (eV) and relative areas of the components (%) of Cu $2p_{3/2}$, Cu LMM, and O 1s peaks for CuO-ethanol samples

Core excitation	**Doublet No.**	**CuO-raw**		**CuO100**		**CuO200**		**CuO300**		**CuO400**	
		BE (eV)	Area (%)	BE (eV)	Area (%)	BE (eV)	Area (%)	BE (eV)	Area (%)	BE (eV)	Area (%)
Cu $2p_{3/2}$	1	930.9	1.0	931.6	5.6	931.4	5.3	931.3	3.4	931.5	4.5
	2	932.8	33.8	932.9	43.2	932.8	57.6	932.8	49.9	932.9	59.7
	3	934.0	44.9	933.7	36.0	933.4	25.3	933.6	25.4	933.5	23.9
	4	935.6	20.3	935.7	15.2	935.3	11.8	935.2	21.3	935.1	11.9
Cu LMM	1	568.9	100	568.7	41.4	568.4	35.6	568.3	30.7	568.2	23.6
	2	--	--	570.3	58.6	570.3	64.4	570.2	69.3	570.3	76.4
O 1s	1	529.9	45.2	530.6	47.8	530.8	45.0	530.9	28.4	531.0	32.9
	2	531.5	18.1	532.1	33.3	532.1	26.4	532.1	39.8	532.1	37.8
	3	533.0	32.9	533.7	15.3	533.2	22.1	533.3	26.7	533.3	20.6
	4	534.8	3.8	535.2	3.6	535.7	6.5	535.8	5.1	535.7	8.7

Table 4. Results of gas chromatographic analyzes of Cu-ethanol and CuO-ethanol samples before and after irradiation with different laser fluences. The formation of C_2H_4 and C_2H_6 and the increase in the content of CH_4 and CO show the partial dissociation of the solvent during the PLIS process.

Gas	Unit	Before irradiation		After irradiation			
		Cu-ethanol	CuO-ethanol	Cu100	Cu200	CuO200	CuO400
CO_2	PPM	704.3	705.4	674.8	641.5	762.8	845.5
CO	PPM	1.9	1.9	10.4	14.8	29.5	208.9
O_2	%	20.68	20.70	20.71	20.69	20.61	20.47
CH_4	PPM	2.9	2.6	3.1	3.7	7.8	35.8
C_2H_6	PPM	0.0	0.0	0.8	2.7	2.6	14.7
C_2H_4	PPM	0.0	0.0	0.0	7.3	1.3	67.5

Table 5. Amounts for maximum size of particles that can be melted, average size of final agglomerates, average size of particles, and probability of probe

Sample code	Maximum size of particle that can be melted	Average size of resulted agglomerates	Average size of particles	X			
				Without phase transition	With Cu » CuO transition	With Cu » Cu_2O transition	With CuO » Cu_2O transition
Cu50	250	450	250	1.54	1.28	1.25	-
Cu100	400	320	313	1.80	1.53	1.50	-
Cu150	550	400	390	2.11	1.83	1.79	-
Cu200	700	500	470	2.35	2.05	2.00	-
CuO100	250	400	392	1.92	-	-	1.87
CuO200	450	550	534	2.38	-	-	2.33
CuO300	600	680	559	2.47	-	-	2.42
CuO400	750	820	734	2.97	-	-	2.92